History of volcanism and sedimentation synchronous with plutonism during Rhyacian in Serra das Pipocas Greenstone Belt, Borborema Province, NE Brazil

Herdivânia Pires de Sousa[a],[*],[1], Clóvis Vaz Parente[a],[1], Christiano Magini[a],[1], Dillano Rodrigues Bastos Ximenes[a],[1], Elton Luiz Dantas[b], Renaud Caby[c], Cecílio Aguiar Rosa Júnior[a],[1]

[a] Departamento de Geologia, Universidade Federal do Ceará - UFC, Campus do Pici – Bloco 912, CEP 60440-554, Fortaleza CE, Brazil
[b] Instituto de Geociências, Universidade de Brasília - UnB, Campus Universitário Darcy Ribeiro, Brasília, DF 70910-900, Brazil
[c] Université de Montpellier II - CNRS, Place E.Bataillon, 34 095 Montpellier Cedex 05, France

ABSTRACT

The Serra das Pipocas Greenstone Belt is one of the rare Paleoproterozoic greenstone belts within the Borborema Province. It is on the west border of the Archean/Paleoproterozoic Nucleus (Cruzeta and Mombaça Complex) of the Ceará Central Domain, northern portion of the Borborema Province. The Serra das Pipocas Greenstone Belt has an elongated sigmoidal shape encompassing about 1000 km^2 of the Ceará Central Domain. It consists of a meta-volcanosedimentary sequence formed by metasedimentary psammitic-pelitic-marly rocks and interleaved metaultramafic and metamafic rocks, represented by chlorite-anthophyllite-actinolite/tremolite schists and amphibolites. Layers of metatuffs, metabasic, meta-acid sills (metadacites), metacherts, gondites and banded iron formations occur within the metamafic rocks. Actinolite, metagabbro, metadiorite bodies, metabasic dike, Neoproterozoic metagranodiorites and leucogranites crosscut the metavolcanosedimentary sequence. Close to the borders of metagranodioritic bodies (zircon U–Pb 2181 ± 4.4 Ma), the metavolcanosedimentary sequence is hydrothermally altered. The metaultramafic rock (chlorite-anthophyllite-actinolite/tremolite schist) contains high MgO (> 18 wt%), low alkali (≤1 wt%) and TiO$_2$ (< 0.8 wt%) and Al$_2$O$_3$/TiO$_2$ ratios between 9.94 and 27.26, with a mean value of 17.13. Values of (Gd/Yb)$_N$ vary between 1.00 and 1.88, which attest affiliation with komatiite protoliths, between the Munro and Barberton types. The amphibolites are usually fine-grained and depleted in ΣREE (33.14–45.02 ppm), with low (La/Yb)$_{CH}$ values (0.74–3.82). This reflects weak LREE enrichment in relation to HREE, and no Ce and Eu anomalies [(Eu/Eu*)$_n$ between 0.98 and 1.04]. Such patterns are similar to T-MORB (1.7–4.3). Additionally, some mafic-ultramafic metaplutonic rocks present chemical composition similar to their volcanic counterparts, and this may indicate cumulates or sills contemporary to this sequence. Zircon U–Pb dating using LA-ICP-MS of three distinct metadacite occurrences (western border: 2234 ± 13 Ma, eastern border: 2212 ± 13 Ma, and central portion: 2156 ± 45 Ma) and metagranodiorites (2181 ± 4.4 Ma) indicates that the sequence was formed during the Rhyacian/Orosirian and later affected by late Neoproterozoic.

1. Introduction

Paleoproterozoic metavolcanosedimentary sequences of the greenstone belt type are recorded in several cratonic domains worldwide, within extensional or intracratonic tectonic basins of the back-arc type. Some examples are the Eburnean-Birimian Greenstone Belt of the West African Craton (Baratoux et al., 2011; Kock et al., 2011); the Vila Nova do Escudo, Pastora-Barama Mazaruni, and Paramaka das Guianas greenstone belts of the Amazonian Craton (Vanderhaeghe et al., 1998; Rosa-Costa et al., 2006; McReath and Faraco, 2006); metavolcanosedimentary sequences of the Aurizona Group of the São Luís Craton (Klein et al., 2005, 2008), and the Rio Itapicuru and Rio Capim greenstone belts of the São Francisco Craton (Silva et al., 2001; Mello et al., 2006; Costa et al., 2011; Oliveira et al., 2011). In the Borborema

Fig. 1. A. Borborema Province location in South American Plate. B. Pre-drift reconstruction of NE Brazil and NW Africa in late Neoproterozoic and early Paleozoic time (Caby, 1989). C. Septentrional Borborema Subprovince and location of the study area in the Archean Nucleus of the Ceará Central Domain (modified after Cavalcante, 1999; Brito Neves et al., 2000; Delgado et al., 2003; Arthaud et al., 2008; De Wit et al., 2008). Main shear zones: TBSZ, Transbrasiliano (Sobral– Pedro II); TSZ, Tauá; SISZ, Sabonete– Inharé; SPSZ, Senador Pompeu; OSZ, Orós; JSZ, Jaguaribe; PASZ, Portalegre; JCSZ, João Câmara; ASZ, Aiuába; FBSZ, Farias Brito; PSZ, Patos. RGF, Rio Groaíras fault.

Province the Algodões supracrustal sequence (Martins et al., 2009; Costa et al., 2015), the Serra Caiada Greenstone (Dantas, 2009) and, in São Francisco Craton, the Mundo Novo Greenstone Belt (Barbuena, 2017) are highlighted.

In the Ceará state, the main Archean/Paleoproterozoic nucleus that encompasses such metavolcanosedimentary sequences is located in the central-southern portion of the Ceará Central Domain (CCD) (Fig. 1). This domain was initially named Troia Massif by Brito Neves (1975a,b). Arthaud et al. (2008) divided it as Cruzeta and Mombaça Archean

complexes, both constituted by migmatized grey orthogneisses exhibiting compositional banding with the predominance of tonalitic/ granodioritic bands over granitic bands. According to Fetter (1999), these rocks yielded U-Pb ages in the 2.8–2.7 Ga interval, and Sm-Nd model ages between 2.9 and 3.04 Ga and negative ε_{Nd}. Araújo et al. (2017) obtained U-Pb zircon ages between 2.85 and 2.77 Ga for the protolith of the Mombaça Complex Gneisses.

According to Caby and Arthaud (1986), Caby et al. (1995) and Arthaud et al. (2008), boudins of layered or massive mafic-ultramafic

bodies are frequent in these terranes, some of which mineralized in stratiform chromite and PGEs. Minor occurrences of supracrustal rocks are constituted by thin lenses of banded iron formation, associated with amphibolite, tourmalinite, paragneiss that, together with the orthogneiss, constitute the greenstone-gneiss association.

The Paleoproterozoic terranes surround the Archean block in an irregular shape. They include several lithologic associations grouped in three distinct units (e.g. Arthaud et al., 2008): i) a gneissic-migmatitic complex, dominated by orthogneisses of tonalitic to granodioritic composition, yielding U-Pb zircon ages between 2.11 and 2.19 Ga (Fetter, 1999); ii) the Madalena Suite, represented by quartz-dioritic rocks yielding U-Pb ages between 2.15 and 2.2 Ga (Castro, 2004), and iii) the Algodões Unit, characterized by supracrustal sequences constituted by basic metavolcanic rocks (amphibolites and garnet amphibolites), metaultramafic rocks of tholeiitic nature, with ε_{Nd} values (at 2.0 Ga) from 7.6 to 7.9, and whole-rock Sm-Nd isochron of 2.06 $\pm$ 0.1 Ga, besides a variety of metasedimentary rocks, including iron and manganese formations (Arthaud and Landim, 1995; Martins et al., 2009; Arthaud et al., 2008). Fetter (1999) and Fetter et al. (2003), noted that the Paleoproterozoic intrusive terranes resulted from the accretion of island arcs (ages between 2.1 and 2.15 Ga) around a small Archean nucleus.

Pinéo and Costa (2013) and Costa et al. (2015), using airborne geophysical, geochemical and geochronological data, proposed new limits between the Neoarchean/Paleoproterozoic nucleus and the Paleoproterozoic Ceará Central Domain Gneissic Complex. As a result, an increase in the area of Paleoproterozoic terranes and Archean terranes were observed (Fig. 2).

The Serra das Pipocas Greenstone Belt (SPGB) is located in the CCD central-southern portion, within the Cruzeta gneissic-migmatitic complex. Cavalcante et al. (2003) also included SPGB in the Cruzeta Complex, referring to it as Troia Unit of Archean age. It is composed of metagabbros, metabasalts, metaultramafic rocks, metadiorites and basic metatuffs associated with schists, metacherts, iron formations and kyanite-bearing mica schists.

Albano and Sousa (2005) and Rosa Júnior (2012), based on preliminary petrographic and geochemical analyses, attributed metabasaltic komatiitic affiliation to the metaultramafic rocks. Together with the host rocks, the sequence was named Serra das Pipocas Greenstone Belt.

This paper presents a summary of the main geological, petrographic, geochronological and geochemical features of the lithological associations, in particular of the metaultramafic rocks, which characteristics are quite similar to those of the Paleoproterozoic greenstone belt sequences.

2. Regional setting

Serra das Pipocas Greenstone Belt (SPGB) is located in the Ceará Central Domain, Northern portion of Borborema Province (Fig. 1), which is interpreted as a complex region of tectono-stratigraphic domains affected by several tectono-metamorphic episodes, between the Archean and the Neoproterozoic (Almeida et al., 1977, 1981; Arthaud et al., 2008; Ganade et al., 2016; Costa et al., 2018).

Three tectonic segments or terranes are individualized in the Borborema Province, according to geologic and geochronological characteristics. They are limited by two EW-trending, dextral megatranscurrent faults (Patos and Pernambuco lineaments) that divide the Borborema Province in the Septentrional Borborema, Transversal Zone and Meridional Borborema subprovinces (Van Schmus et al., 1995; Arthaud, 2007).

The Septentrional Borborema Subprovince is located north of the Patos Lineament and encompasses the study area. Mega-shear zones activated at the end of the Brasiliano orogeny divide this subprovince in Médio Coreaú, Ceará Central and Rio Grande do Norte geotectonic domains (Fetter, 1999; Brito Neves et al., 2000; Delgado et al., 2003; Amaral, 2010).

The Archean/Paleoproterozoic terrains of the Ceará Central Domain (CCD) are characterized by two chronostratigraphic associations: (1) the Archean basement, represented by the Cruzeta Complex, composed of migmatitic banded gneisses of tonalite and granodiorite composition interlayered within remnants of pelitic metasedimentary rocks, calc-silicate rocks, quartzite, and banded iron formation. Intercalations of mafic and sometimes chromite-bearing ultramafic rocks are common (Arthaud et al., 2008, 2015) and (2) Paleoproterozoic accretionary terranes that encompass poorly differentiated granitic bodies (the Madalena Suite – Castro, 2004, and the São José da Macaoca Unit – Arthaud et al., 2008); the TTG-type Sítio dos Bois and Cipó orthogneisses (Cavalcante et al., 2003); mafic-ultramafic rocks (the Boa Viagem Mafic-Ultramafic Intrusive Suite – Parente et al., 2008, and the Troia Mafic-Ultramafic Complex – Costa et al., 2015); metavolcanosedimentary sequences (the Algodões Sequence – Martins et al., 2009), and the Canindé Complex (Torres et al., 2007), and Serra das Pipocas Greentone Belt belongs to this chronostratigraphic sequence (Fig. 2) (Veríssimo et al., 2016).

3. Materials and methods

The combined use of airborne geophysical data and satellite data (Landsat 8) allowed the delimitation of different mafic-ultramafic bodies, geological domains and regional structures. From magnetometric (ASA) and gamma-spectrometric (K, eU, eTh) data, a Mafic Index (MI) was generated. MI is a useful technique for the individualization of mafic and ultramafic bodies (Pires and Moraes, 2006).

A hundred thin sections and 20 polished sections were described focusing on silicates and ore minerals. The scheme of Whitney and Evans (2010) was used for the abbreviation of mineral names.

Twenty-two mafic and ultramafic rock samples were analyzed for major elements (wt.%) and trace and rare-earth elements (in ppm) at the Acme Analytical Laboratories Ltd., adopting the analytical procedures 4A and 4B, described in www.acmelab.com. The geochemical diagrams were drawn using the GCDkit 3.0 software (Janoušek et al., 2008).

Six samples were analyzed by the U-Pb method and ten by the Sm-Nd method at the UnB Geochronology Laboratory. The sample preparation for the U-Pb analyses, were done at the UFC Sample Preparation and Geotechnical Laboratory according to the following procedures: pulverization using a jaw crusher; classification using 80- and 120-mesh sieves; panning and demagnetization using a Frantz separator. Zircon grains were selected from the non-magnetic fraction by means of a binocular stereoscope and mounted in epoxy resin and polished. The isotopic analyses were then performed using the LA-ICPMS equipment of the UnB Geochronology Laboratory, according to the methodology described in Buhn et al. (2009).

Sm-Nd analyses were performed using the mass spectrometry method described in Gioia and Pimentel (2000). The powder of whole-rock samples (50 mg) was mixed with a ^{149}Sm-^{150}Nd spike acid solution and dissolved in Savillex beakers. The cationic-exchange technique was used for Sm and Nd extraction in Teflon columns containing Ln-Spec resin. Sm and Nd samples were deposited on rhenium double filaments and the isotopic measurements were performed using a Triton mass spectrometer in static mode (Dantas et al., 2002).

4. Geological setting and petrography

SPGB (350 km^2) belongs to a series of Paleoproterozoic supracrustal sequences of volcanosedimentary origin associated with TTG terranes (Fig. 2). The contact between these units is made by thrusting zones. Therefore, the Cruzeta Complex overthrusts SPGB and the Independência Unit overthrusts the SPGB (Fig. 3).

SPGB is composed by psammitic-pelitic-marly sequence interleaved with metaultramafic, metamafic and meta-acid rocks, represented by chlorite-anthophyllite-actinolite/tremolite schists, amphibolites and metadacites, respectively. Intrusive metagranitic bodies occur as sheets, and metamafic dikes represented by actinolitites and hornblendites are also common in the sequence. Therefore, it is possible to individualize in SPGB four lithologic groups: i. metasedimentary rocks; ii. metaultramafic rocks; iii. metamafic, intermediate and acid rocks; iv. intrusive rocks.
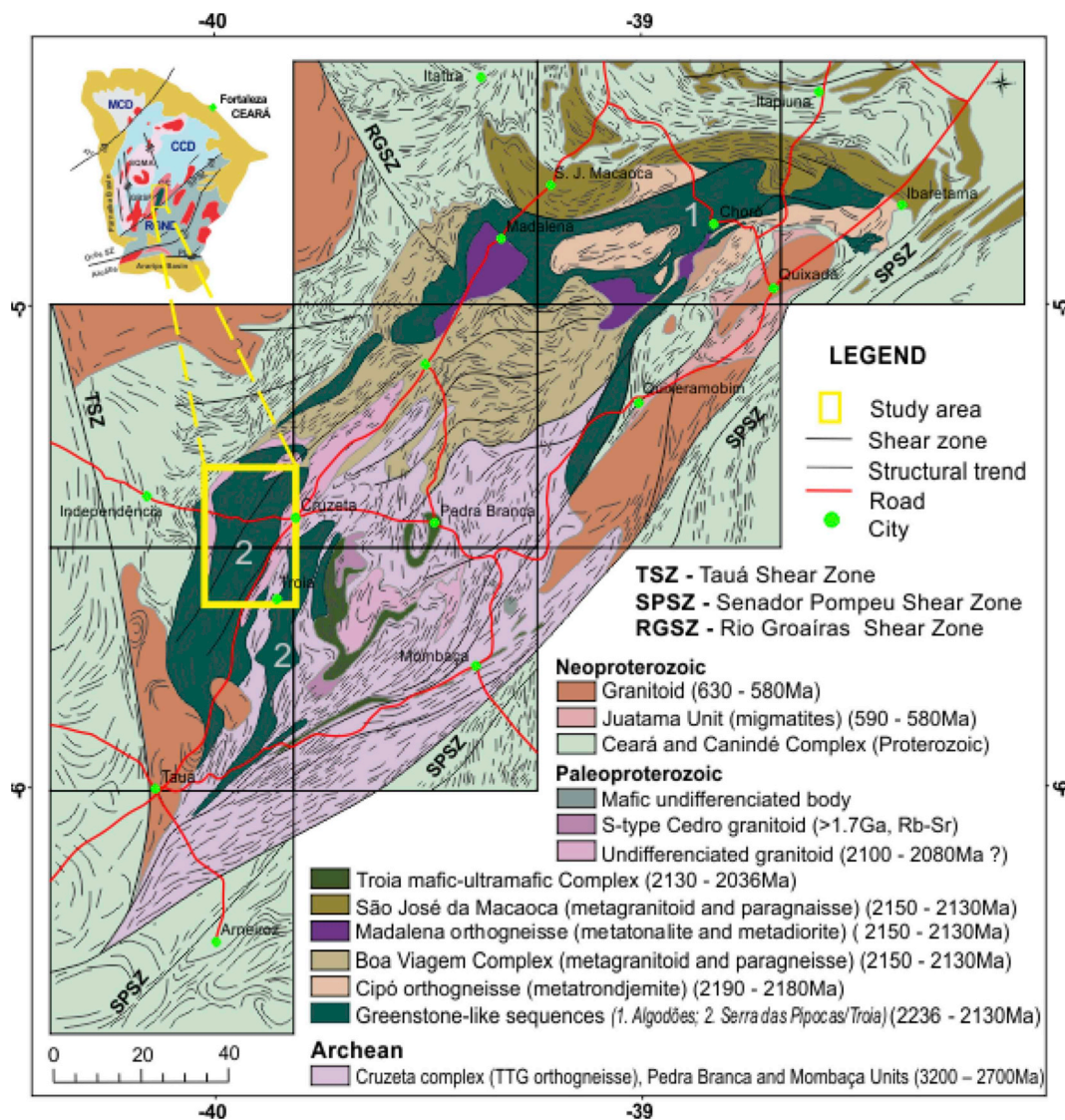
Fig. 2. Simplified geological map of the Archean/Paleoproterozoic Terranes of the Ceará Central Domain including the location of the Serra das Pipocas Greenstone Belt (Costa et al., 2015).

The **metasedimentary rocks** are represented by metapelites and metapsammites, with occasional layers of centimeter-thick calc-silicate rocks, in which the primary structures (S_0) are still preserved. They are distributed throughout the sequence, with the metapsammites closer to the borders and the metapelites in the central portion of the sequence, indicating decrease of sediment transport energy from the border to the center. The metapsammites are represented by feldspatic gneisses derived from meta-arkoses, whereas the metapelites are characterized by garnet schists that may contain graphite and syn- or late-tectonic kyanite porphyroblasts. Close to the thrust zones, 5 cm-sized kyanite porphyroblasts developed in the metasedimentary rocks. Garnet micro-inclusions may be present in the kyanite porphyroblasts. These characteristics indicate a sedimentary protolith deposited in calm, deep and reduced waters.

The **metaultramafic rocks** are massive or stratified (Fig. 4A and B). Some bodies present intercalations of basic metatuffs and tourmaline-bearing meta-exhalites, which indicates that part of the metaultramafic rocks are metamorphosed flows. They occur as discontinuous lenses, mainly concentrated in the western border of the sequence, where they extend for about 20 km. Individually, the metaultramafic lenses are less than 30 m thick, but as a whole, they can reach 300 m of thickness. The metaultramafic rocks overlap or are intercalated with acid metavolcanic and psammitic-pelitic rocks. They consist of fine-grained anthophyllite-chlorite-actinolite/tremolite schists, with or without radial

texture or banding, and are strongly chloritized as a result of metamorphic and/or hydrothermal transformations. Under the microscope, the rock types display nematoblastic texture. The mineral assemblage is actinolite/tremolite (70–75 wt%), chlorite (15–20 wt%), and anthophyllite (10–15 wt%). Ilmenite (1–5 wt%), rutile (1–5 wt%), apatite (1–5 wt%) and chromiferous magnetite (1–3 wt%) occur as accessory minerals in the less magnesian terms (Fig. 4C and D).

The **metamafic rocks** extend for about 30 km along the NE-SW direction and are 500-m to 1-km wide (Fig. 5A and B). They consist of massive and/or stratified garnet-rich amphibolites, sometimes associated with basic metatuffs, metacherts, and banded iron formations, and concentrate predominantly in the middle portion of the SPGB sequence. They can also be found in the eastern border of SPGB as massive amphibolites (Fig. 5C e 5D) and hydrothermally altered basic flows (Fig. 5G e 5H). They occur as massive slabs or blocks, exhibiting shallow dipping foliation (15°–20°), locally modified by steep foliation associated with shear. The amphibolites are fine to medium grained, banded and composed of hornblende (55–65 wt%), plagioclase (30–40 wt%), garnet (0–5 wt%), titanite (1 wt%), ilmenite (1 wt%), apatite (1 wt%), epidote (0–1 wt%) and secondary calcite (0–1 wt%). They present nematoblastic to granonematoblastic texture and garnet porphyroblasts (Fig. 5C and D). Another underwater volcanic structure preserved in the SPGB is pillow lavas (Fig. 5E and F).
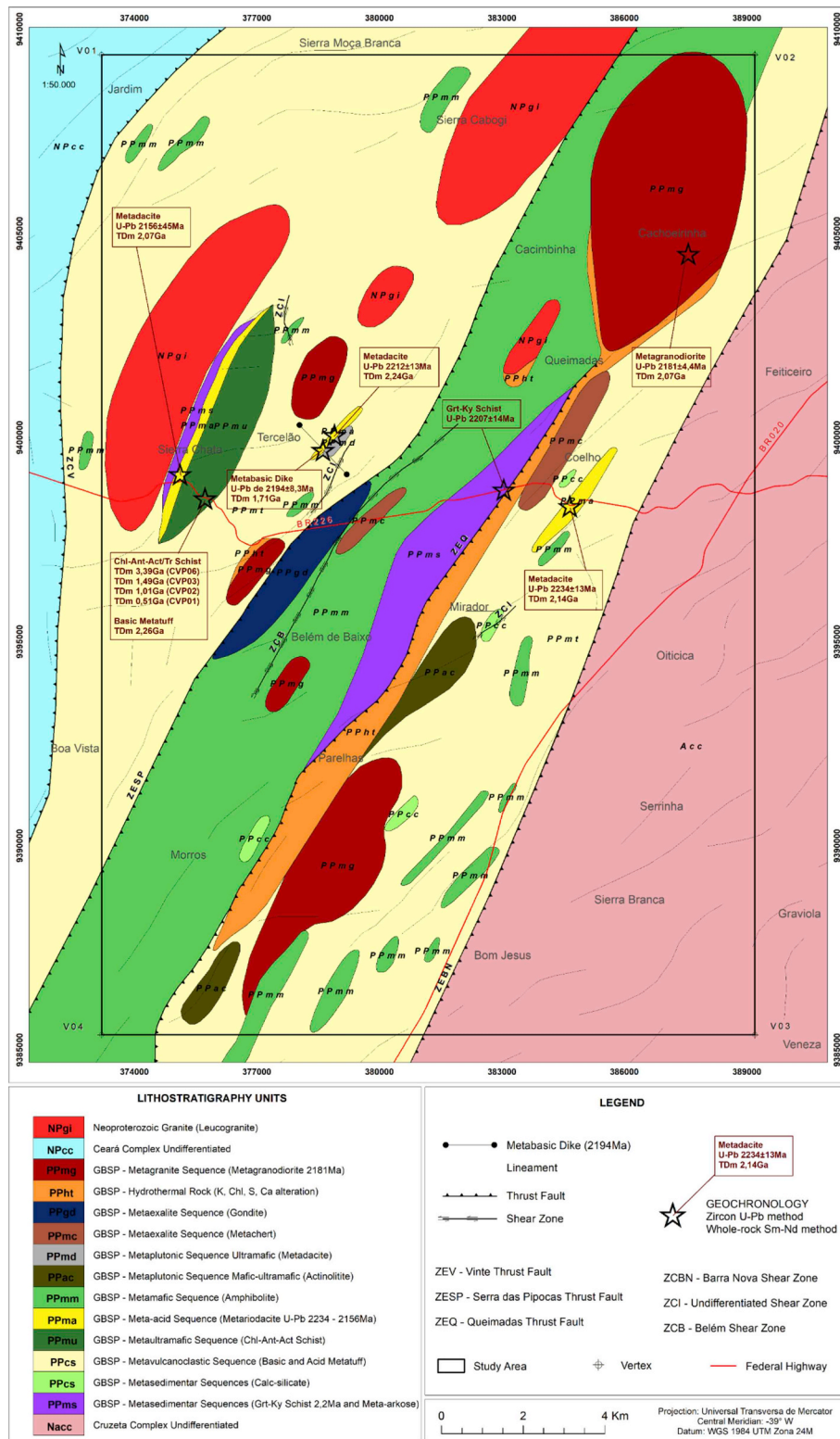
Fig. 3. SPGB geological map and geochronologic data of volcanic and plutonic lithologies.

Basic and acid metatuffs, metacherts, gondites and banded iron formations occur intercalated with the metamafic rocks, which are strongly hydrothermally altered at the borders of the metagranodioritic bodies of the eastern portion, close to the Queimadas thrust zone.

The **hydrothermally altered basic flows** has fine granulation and banded structure (Fig. 5G). The intercalation is demarcated between hornblende and plagioclase, sometimes with tourmaline (Fig. 5H).

The **intrusive rocks** that crosscut the metavolcanosedimentary sequence are: i. a metabasic dike; ii. plutonic mafic-ultramafic rocks, and iii. granitic rocks.

The **metabasic dike** trends 110°Az and is 30 cm thick and 50 m long. It crosscuts the tectonic banding of the mafic-ultramafic metavolcanic rocks, metadacites and metatuffs (Fig. 6A and B), which are metamorphosed to the amphibolite facies. The dike is volcanic and presents
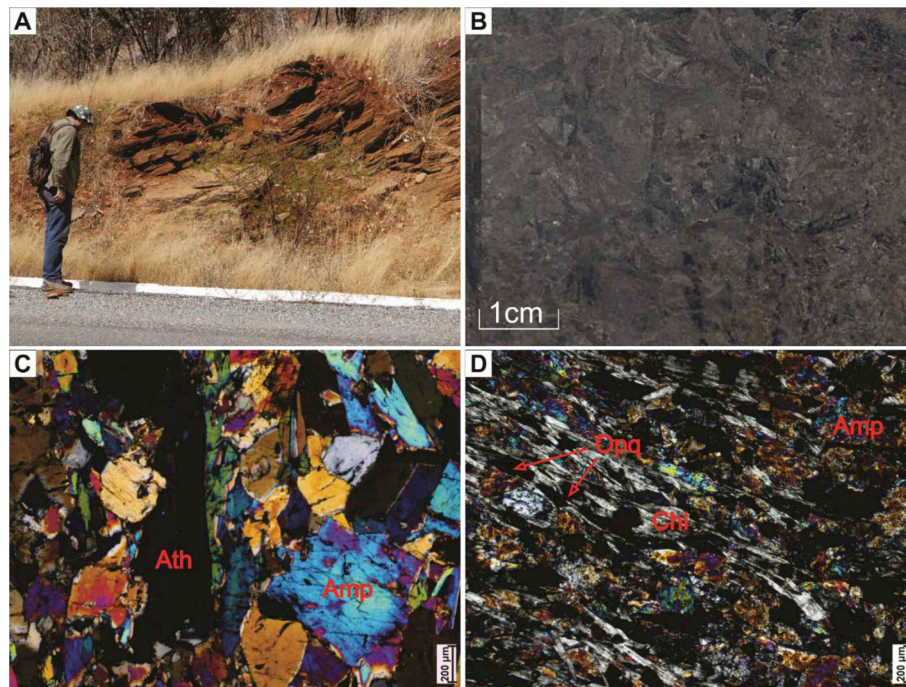
Fig. 4. A. Roadcut outcrop of one of the metaultramafic flows intercalated with basic metatuffs and/or meta-exhalites containing garnet and tourmaline. B. Sample of the anthophyllite-chlorite-actinolite/tremolite schist with radial habit crystals. C and D. S_{n+2} foliation marked by chlorite and opaque minerals (crossed nicols).

aphanitic texture and mineral assemblage formed by plagioclase (50 wt %), phlogopite (35 wt%), actinolite (15 wt%) and apatite (1 wt%). Some of the actinolite crystals appear to be pseudomorphs after clinopyroxene.

The **intrusive mafic-ultramafic rocks** are exposed as meter-to-decameter-sized, boulders. They are composed of actinolitites, gabbros and metadiorites. They occur in the eastern portion of the study area, close to the amphibolitized metabasic-ultrabasic rocks, which suggests they should be sill-like intrusive bodies related to a cumulate phase dismembered during the mafic-ultramafic magmatism. The actinolitites are greenish, melanocratic, and of varied grain size, from very coarse-to medium-grained. They may represent distinct magmatic pulses, which are common in layered complexes. They are composed of actinolite (90 wt%), and minor plagioclase (5 wt%), representing an intercumulus phase, titanite (2 wt%), epidote (2 wt%) and apatite (1 wt%) (Fig. 6C, D and 6E). This assembly suggests that the protoliths were pyroxenites with plagioclase, the secondary minerals are not rich in magnesium.

The **metagranitic rocks** that crosscut SPGB are represented by dikes and stocks of granodioritic to granitic composition. Some occur as anastomosed sills, suggestive of mixing-mingling between mafic and felsic magmas (Fig. 6F).

5. Deformation and metamorphism

The rocks from the Cruzeta Complex and the Serra das Pipocas Greenstone Belt have distinct tectonic and metamorphic histories. The Cruzeta Complex present age of TTG crystallization of 2.7Ga. The main structures are dominant NE-SW-trending low-angle foliation (Sn), dipping from 20° to 60° to southeast, and regional-scale open folds (Fetter, 1999; Silva et al., 2002; Ganade et al., 2017). The foliation is usually marked by metamorphic banding, given by alternating mafic- (biotite and amphibole) and felsic-rich bands (quartz, plagioclase and potassic feldspar), developed under high amphibolite-facies to partial melting conditions during a Paleoproterozoic event.

Kyanite metaporphyroblast observed in the interface of the metapelitic sequence of the SPGB with the migmatized rocks of the Cruzeta Complex suggests that the contact between these units is tectonic, marked by nappes systems during Brasiliano orogeny.

6. Geochemistry

Out of the 22 analyzed rock samples, nine correspond to metaultramafic rocks (chlorite-anthophyllite-actinolite/tremolite schist), four to metamafic rocks (amphibolite), seven to meta-intrusive rocks (metabasic dike and actinolitite), and two to metavolcaniclastic rocks (basic metatuff) (Table 1).

The samples selected for analysis, in particular those of metaultramafic and metamafic rocks, are deformed, metamorphosed and partially hydrothermally altered. For this reason, chemical parameters were used to test the mobility of certain elements in order to ensure the classification, magmatic affiliation and tectonic setting of the rock types (Polat and Hofmann, 2003; Condie, 2015).

In the binary diagrams involving immobile elements (Zr vs. Ti) (Fig. 7A), a strongly positive trend is observed, indicating that these elements did not undergo post-deformational modifications. However, when the correlation indexes between mobile and immobile elements are used (Zr vs. K; Zr vs. Na$_2$O; Zr vs. MgO) (Fig. 7B, C and 7D), a higher dispersion of the data is observed, with a weak positive correlation, which is more pronounced in the metaultramafic rocks, suggesting a higher mobility of potassium, sodium and magnesium. This is attested by the correlation factor (r): the ultramafic metavolcanic rocks present strong positive correlation between Ti vs. Zr (r = 0.99), attesting the immobile character of these elements and a weak positive correlation between K$_2$O vs. Zr (r = 0.32), Na$_2$O vs. Zr (r = 0.39), and negative correlation between MgO vs. Zr (r = −0.59), which shows that K$_2$O and Na$_2$O contents and, to a lesser extent, MgO contents, were modified. Due to this mobility and the correlation factor, it was decided to interpret the data of s less or immobile elements as Zr, Ti, Nb and Y and ETR's.

6.1. Petrochemical characterization

Applying the diagrams in an inter-elemental way, the possible protoliths, their magmatic affiliation and the tectonic setting can be classified in the TAS diagram (SiO$_2$ vs. Na$_2$O + K$_2$O) by Le Bas (2000) (Fig. 8A). Excepting the metabasic dike, which yields Na$_2$O + K$_2$O content of 6.58 wt% and plots in the trachyandesite basalt field (alkaline series), the other samples plot in the basalt and picrobasalt fields
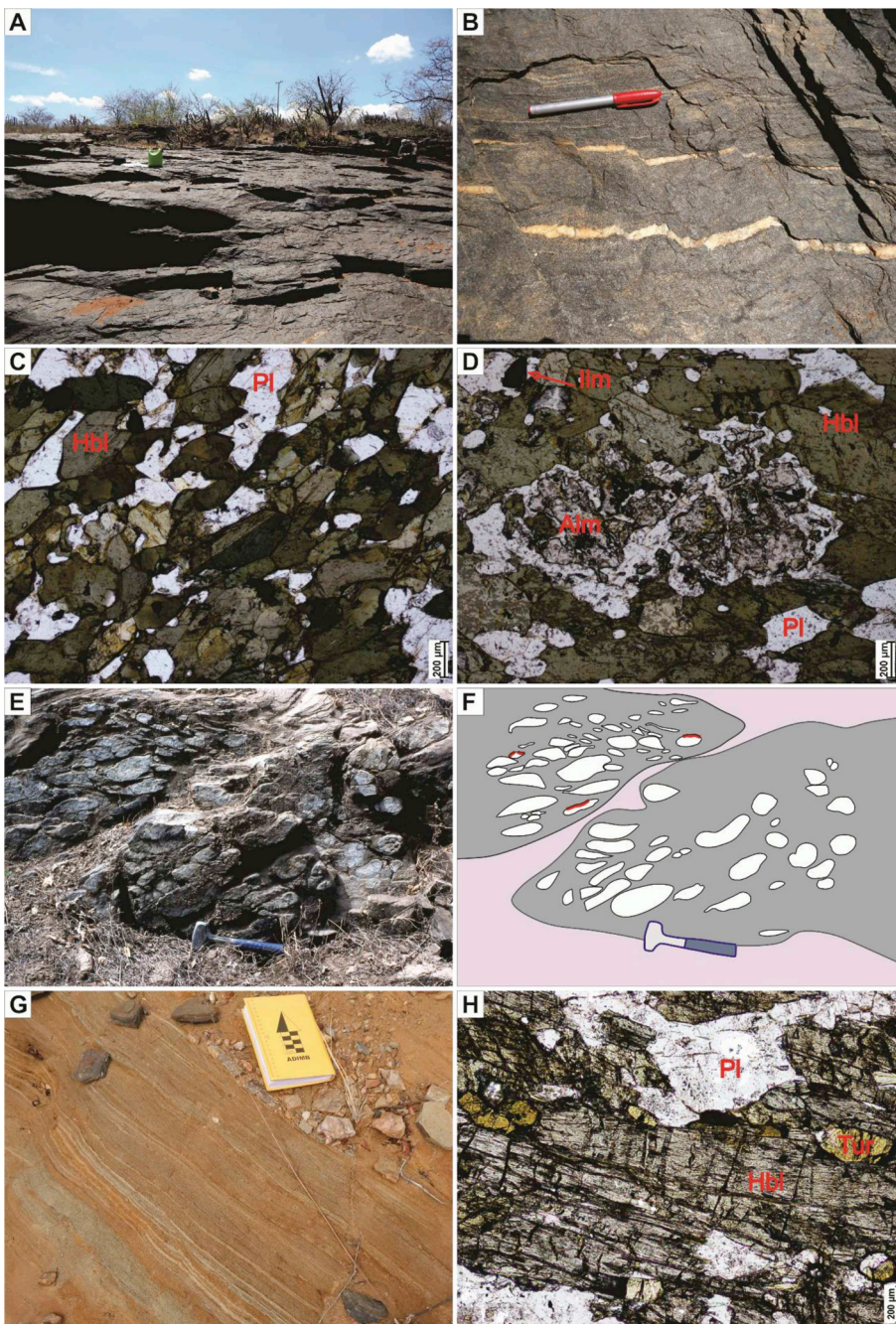
Fig. 5. A. Metabasalt slab in drainage net exhibiting low-angle foliation, with or without garnet-rich portions. B. Microfaulted quartz veins associated with the metabasic flows. C. Granonematoblastic texture of the amphibolite (natural light). D. Xenoblastic garnet (natural light). E. Metapillow type structure represented by subrounded to subangular pillow breccias. F. Breached metapillow graphic with cooling border (highlighted in red). G. Tourmaline-bearing facies associated with metamafic flows. H. Mineral assemblage constituted by plagioclase, hornblende and tourmaline, identified in basic flow. (For interpretation of the references to colour in this figure legend, the reader is referred to the Web version of this article.)

(subalkaline/tholeiitic series). In the TAS diagram by Le Bas (2000), the magnesian schists cluster mainly in the field of the komatiitic basalt protoliths (high MgO ≥ 18 wt% and low TiO$_2$ < 0.80 wt%), whereas the amphibolite, basic metatuff and some actinolite plots in the basalt, boninite and meimechite field.

In a similar classification diagram using immobile elements (Zr/Ti vs. Nb/Y), (e.g. Winchester and Floyd, 1977), recently modified by Pearce (2014) (Fig. 8B), it was observed that, excepting the actinolitite, that plots in the boundary between alkaline and subalkaline basalts field, and the metabasic dike that plots between the trachyandesite and the alkaline basalt fields, the other samples plot in the tholeiitic basalt field. The clustering of the samples in the same field (basalts) in both immobile (Zr/Ti vs. Y/Nb) and mobile (TAS) element diagrams also indicates that SiO$_2$ was not modified.

In the AFM diagram by Wager and Deer (1939, in Miyashiro, 1975), excepting the metabasic dike, all samples plot in the tholeiitic series

field, including a total iron increase for the most differentiated basic terms. It is worth noting that in this diagram there is no field of komatiitic basalts.

In the cationic diagram by Jensen (1976) (Fig. 8C) all the metaultramafic rocks (magnesian schists and actinolitites) fall in the komatiitic basalts field. In turn, the amphibolites preferentially plot in the high-Fe tholeiitic basalt field. The dike plots in the transition field between komatiites and high-Mg tholeiitic basalts.

The magnesian schists also exhibit moderate Al$_2$O$_3$/TiO$_2$ ratios (9.94–27.26), with a mean value of 17.13, and (Gd/Yb)$_N$ between 1.00 and 1.88, which allows one to consider them as originating from komatiitic basalts between Munro and Barberton types (Fig. 9A, B and 9C). The (plutonic) actinolitites are treated as related to a cumulated phase dismembered during the mafic-ultramafic magmatism.

Additionally the magnesian schists present ΣREE = 16.57–53.23 ppm, horizontal HREE patterns, and (La/Yb)$_N$ between 1.13 and 8.33 (Fig. 10A),
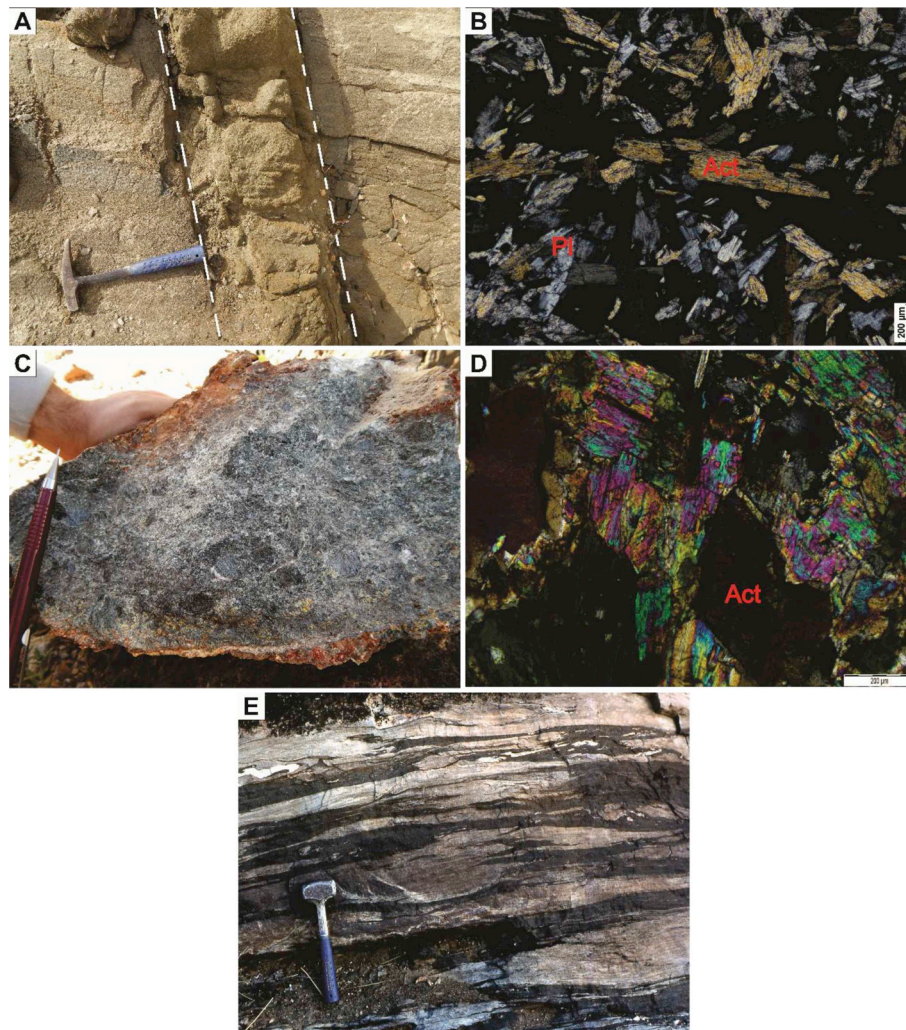
Fig. 6. A. Metabasic dike discordantly crosscutting the metadacite. B. Thin section of the metabasic dike showing elongated actinolite laths (crossed nicols). C. Metamafic rock with amphibole porphyroblast replacing cumulus pyroxene. D. Thin section of the actinolitite exhibiting actinolite porphyroblasts (crossed nicols). E. Deformed mafic and felsic sill.

which indicates a slight LREE enrichment in relation to HREE in some samples, resembling E-type MORB. They show a slightly negative Ce anomaly and weak positive Eu anomaly $[(Eu/Eu^*)_N = 0.83–3.52]$. The highest Eu anomaly is yielded by a single sample (DRI-132A), which may reflect hydrothermal alteration processes.

In the chondrite-normalized multi-element diagram by Thompson (1982), the magnesian schists show negative Ti, Nb, Ta, Sr, Rb and K anomalies and positive Ba and La anomalies (Fig. 10B). Excepting the negative Ti anomaly that can indicate depleted mantle, the other Sr, Rb, K, Ba and La anomalies can be associated with either alteration processes or crustal contamination. This is observed in the Th/Yb vs. Nb/Yb diagram by Pearce (2014), a replacement for the Th-Hf-Ta diagram by Wood et al. (1979).

The lithological groups present a slight enrichment of LREE, whereas the HREE are stable, in the La-Lu series. The lines between the same lithologies are parallel and exhibit similar pattern to mantellic sources for ultramafic rocks (amphibolites and chl-ant-act schist). ε_{nd} values vary from -5 to $+5$. The ETR + Traces Elements indicate that the alkaline elements, accompanying the recrystallization of feldspars and amphiboles, show the largest dispersions were obtained from the actinolitite congruently with the most hydrated rock of the sequence.

The amphibolites yield SiO_2 contents ≤ 52 wt%, low TiO_2 (≤ 1.1 wt%), MgO (7–9 wt%) and $Fe_2O_3^*$ (7–14 wt%) contents. Additionally, TiO_2 increases while MgO decreases. These are characteristics of basic

tholeiitic protoliths, observed in the AFM diagrams by Wager and Deer (1939, in Miyashiro, 1975) and by Jensen (1976) (Fig. 8C). The compatible trace elements exhibit varied contents: Cr from 48.03 to 871.39 ppm and Ni from 52 very coarse-to medium-grained to 222 ppm. The highest Cr and Ni contents can be associated with more primitive basaltic magmas and the lowest with the more evolved terms. The amphibolites also present low HFSE contents, such as Nb $<$ 3 ppm, Zr $<$ 49 ppm, and Ta ≤ 0.3 ppm, characteristic of a depleted mantle source. When comparing the amphibolites with basic rocks of SPGB from the literature and of different tectonic settings, it is observed that they resemble BAAB amphibolites. All the samples show a negative Ti anomaly, which corroborates as indicative of depleted mantle or hydrous mantle (Condie, 2015).

Fig. 10C shows that the amphibolites are depleted in ΣREE (33.14–45.02 ppm), and yield low $(La/Yb)_{CH}$ ratios (0.74–3.82), which attests a weak LREE enrichment in relation to HREE, and no Ce and Eu anomalies $[(Eu/Eu^*)_n = 0.98-1.04]$. Such patterns are more similar to T-MORB (1.7–4.3) than to E-MORB (4.8–6.9) and N-MORB (0.35–1.1).

In the chondrite-normalized multi-element diagram by Thompson (1982) negative Ti, Nb and Ta anomalies are highlighted, which indicate subduction-related (back-arc) settings, and positive Sr, K and Rb anomalies, which reflect alteration processes or crustal contamination (Fig. 10D). According to Puchtel et al. (1998), the assimilation of small quantities of crustal felsic rocks results in an increase in Ba, Pb, U, Th

Table 1

Chemical composition of the main lithological types. The major elements (in w.%) and trace elements (in ppm). (in) intrusive, (ex) extrusive and (exh) exhalative rocks. Fe$_2$O$_3$* is total Fe as Fe$_2$O$_3$.

| | METAULTRAMAFIC | | | | METAMAFIC | | | | | METAMAFIC | |
| | CHL-ANT-ACT SCHIST (ex) | | | | | | | | | AMPHIBOLITE (ex) | |
	CVP01	CVP02	CVP03	CVP06	DRI-132	DRI-132 A	DRI-132 E	HL-73	VI-44	SMSP106A	SMSP21
SiO2 (%)	47.81	53.16	46.77	50.95	46.87	48.97	49.90	52.05	48.01	50.28	50.95
TiO2	0.80	0.18	0.65	0.41	0.64	0.37	0.19	0.23	0.42	1.06	0.49
Al2O3	8.99	3.33	7.63	6.41	6.36	6.92	5.18	5.79	6.70	13.90	13.90
Fe2O3*	12.95	9.82	12.66	11.01	14.69	11.72	11.44	12.56	10.61	13.59	9.89
MnO	0.22	0.20	0.17	0.19	0.19	0.16	0.20	0.18	0.16	0.20	0.17
MgO	14.58	19.07	18.51	20.25	18.57	17.22	21.28	18.59	21.00	7.44	8.78
CaO	11.47	10.74	8.28	6.17	8.82	11.23	7.33	7.95	8.01	9.69	12.11
Na2O	1.03	0.15	0.24	0.37	0.37	0.82	0.28	0.53	0.38	2.83	1.18
K2O	0.14	0.01	0.01	0.01	0.05	0.11	0.03	0.07	0.04	0.15	0.47
P2O5	0.05	0.12	0.02	0.02	0.05	0.07	0.07	0.02	0.10	0.07	0.07
LOI	1.40	2.80	4.40	3.50	2.70	1.70	3.40	1.10	3.80	0.50	1.60
Total	99.69	99.66	99.63	99.62	99.63	99.67	99.61	99.44	99.60	99.76	99.72
Mg#	72.21	81.75	77.14	80.93	74.47	77.22	81.10	77.35	82.04	55.82	67.20
Na2O + K2O	1.17	0.16	0.25	0.38	0.42	0.93	0.31	0.60	0.42	2.98	1.65
Na2O/K2O	7.36	15.00	24.00	37.00	7.4	7.45	9.33	7.57	9.50	18.87	2.51
Cr2O3	0.18	0.02	0.26	0.29	0.24	0.25	0.22	0.32	0.33	0.04	0.13
V (ppm)	294.00	93.00	210.00	159.00	197.00	148.00	120.00	.00	137.00	352.00	194.00
Ba	11.00	3.00	9.00	12.00	37.00	10.00	54.00	1784.00	36.00	35.00	258.00
Co	65.80	54.70	73.20	56.30	84.50	70.30	68.90	59.60	81.30	50.20	50.30
Nb	2.00	1.30	1.70	0.90	1.40	2.40	1.00	0.80	1.20	2.70	1.90
Ni	398.00	469.00	601.00	658.00	668.00	921.00	679.00	447.00	593.00	113.00	222.00
Rb	0.60	0.10	0.10	0.20	0.30	1.60	0.30	0.30	0.50	3.50	4.10
Sr	47.70	22.40	23.00	18.30	28.60	38.30	21.40	60.70	75.90	128.10	428.30
Y	14.70	15.00	17.00	11.00	14.80	10.80	8.80	12.00	8.20	20.00	12.40
Zr	36.40	11.60	30.90	20.60	28.00	16.30	10.60	10.80	19.60	51.60	41.80
Ti	480.97	108.25	391.02	246.67	385.00	222.49	114.32	138.63	252.73	636.83	294.50
Nb/Y	0.14	0.09	0.10	0.08	0.09	0.22	0.11	0.07	0.15	0.14	0.15
Zr/Ti	0.08	0.11	0.08	0.08	0.07	0.07	0.09	0.08	0.08	0.08	0.14
La (ppm)	2.60	2.5	12.20	2.00	4.50	4.50	2.80	2.30	9.30	2.70	7.80
Ce	5.20	5.4	15.00	3.30	5.90	9.50	3.10	3.90	11.60	6.40	15.00
Pr	1.00	1.00	2.87	0.72	1.34	1.50	0.77	0.85	2.07	1.12	2.18
Nd	4.90	5.50	11.90	3.90	6.40	6.70	3.40	4.00	7.70	6.5	9.20
Sm	1.74	1.94	2.63	1.15	1.90	1.50	0.89	1.22	1.65	2.03	1.89
Eu	0.88	0.50	1.00	0.34	0.68	1.40	0.43	0.52	0.52	0.83	0.64
Gd	2.37	2.95	3.05	1.58	2.34	1.72	1.16	1.63	1.69	2.92	2.09
Tb	0.45	0.53	0.58	0.30	0.44	0.32	0.24	0.32	0.28	0.56	0.34
Dy	2.77	3.09	3.33	1.85	2.74	1.82	1.36	2.02	1.57	3.59	2.11
Ho	0.61	0.65	0.70	0.41	0.57	0.41	0.33	0.45	0.32	0.86	0.49
Er	1.66	1.76	1.87	1.29	1.60	1.17	1.01	1.29	0.91	2.38	1.45
Tm	0.25	0.20	0.25	0.18	0.23	0.18	0.14	0.21	0.12	0.37	0.22
Yb	1.57	1.27	1.62	1.18	1.45	1.14	0.81	1.32	0.76	2.50	1.39
Lu	0.21	0.18	0.23	0.18	0.21	0.18	0.13	0.18	0.11	0.38	0.22
Hf	1.10	0.70	0.80	0.60	1.00	0.50	0.40	0.40	0.70	1.40	1.10
Ta	0.10	0.10	0.10	0.10	0.20	0.10	0.20	0.10	0.10	0.30	0.10
Pb	0.10	0.10	0.10	0.10	0.20	0.50	0.10	0.40	0.20	0.10	6.60
Th	0.20	0.20	0.20	0.20	0.20	0.20	0.20	0.20	0.40	0.20	1.20
U	0.10	0.10	0.10	0.40	0.10	0.20	0.10	0.10	0.20	0.10	0.30

9

Table 1 (*continued*)

| | METAULTRAMAFIC | | | | | | | | | METAMAFIC | |
| | CHL-ANT-ACT SCHIST (ex) | | | | | | | | | AMPHIBOLITE (ex) | |
	CVP01	CVP02	CVP03	CVP06	DRI-132	DRI-132 A	DRI-132 E	HL-73	VI-44	SMSP106A	SMSP21
Be	1.00	1.00	4.00	1.00	1.00	7.00	1.00	1.00	1.00	1.00	1.00
Sc	43.00	24.00	28.00	24.00	30.00	23.00	23.00	19.00	27.00	43.00	41.00
ΣREE	71.81	53.67	90.53	44.78	62.90	63.54	41.57	41.41	68.20	79.24	96.32

| | METAMAFIC | | | | | METAPLUTONIC | | | METAMAFIC | | |
| | AMPHIBOLITE (ex) | | METATUFF (exh) | | DIKE (in) | ACTINOLITITE (in) | | | AMPHIBOLITE (ex) | | |
	SMSP30	VI-14B	SMSP109B	SMSP122J	SMSP23B	SMSP45	SMSP88A	VE-22B	VI-109A	VI-12C	VI-65A
SiO2 (%)	52.44	50.10	50.99	53.18	51.03	57.11	53.43	52.35	48.34	51.83	49.50
TiO2	0.38	0.82	1.47	0.68	1.14	0.39	0.31	0.39	0.86	0.48	0.76
Al2O3	15.21	14.48	13.67	14.91	12.99	6.92	8.41	4.46	12.33	7.31	6.01
Fe2O3*	7.58	12.67	15.22	9.81	7.22	7.75	8.89	11.09	13.48	9.77	13.04
MnO	0.13	0.18	0.19	0.19	0.10	0.24	0.15	0.25	0.18	0.17	0.25
MgO	8.59	7.04	6.33	6.93	10.43	13.06	12.67	16.56	9.87	15.31	15.30
CaO	11.01	9.96	8.34	10.74	5.68	10.25	12.08	12.55	12.02	12.41	12.37
Na2O	2.91	2.68	2.46	1.47	3.74	1.68	0.48	0.62	1.00	0.94	0.94
K2O	0.55	0.89	0.17	0.43	2.79	0.30	0.25	0.22	0.22	0.58	0.61
P2O5	0.05	0.10	0.12	0.14	1.07	0.02	0.16	0.075	0.11	0.05	0.17
LOI	0.90	0.80	0.80	1.20	2.90	1.80	2.40	1.00	1.10	0.50	0.50
Total	99.79	99.72	99.76	99.77	99.27	99.67	99.52	99.66	99.65	99.69	99.65
Mg#	72.34	56.18	48.97	61.98	76.92	79.54	76.68	77.51	62.82	78.34	73.03
Na2O + K2O	3.46	3.57	2.63	1.90	6.53	1.98	0.73	0.84	1.22	1.52	1.55
Na2O/K2O	5.29	3.01	14.47	3.42	1.34	5.60	1.92	2.82	4.55	1.62	1.54
Cr2O3	0.05	0.01	0.03	0.11	0.08	0.15	0.22	0.09	0.11	0.30	0.17
V (ppm)	152.00	272.00	436.00	172.00	113.00	134.00	111.00	209.00	272.00	226.00	236.00
Ba	110.00	488.00	162.00	196.00	2637.00	327.00	98.00	48.00	572.00	43.00	39.00
Co	36.60	48.00	43.40	31.00	38.30	69.40	70.20	62.60	61.10	52.60	68.80
Nb	2.00	2.80	3.80	4.10	12.20	2.30	2.80	0.90	3.60	1.90	14.50
Ni	128.00	52.00	71.00	217.00	362.00	137.00	649.00	82.00	256.00	289.00	155.00
Rb	8.20	31.10	4.30	12.50	75.70	2.60	2.40	1.30	3.10	8.50	9.90
Sr	199.40	291.30	83.30	285.40	1191.40	255.70	171.70	111.60	287.90	65.20	64.70
Y	11.90	19.30	36.10	15.80	20.10	16.20	7.50	8.90	21.10	10.90	20.40
Zr	49.90	49.70	83.00	83.80	382.30	34.70	25.80	26.40	59.5	26.00	58.00
Ti	228.23	492.84	883.15	408.49	688.28	234.56	186.69	234.54	517.25	288.58	457.10
Nb/Y	0.17	0.15	0.11	0.26	0.61	0.14	0.37	0.10	0.17	0.17	0.71
Zr/Ti	0.22	0.10	0.09	0.21	0.56	0.15	0.14	0.11	0.12	0.09	0.13
La (ppm)	5.90	5.00	6.90	6.10	76.40	22.40	7.40	2.60	5.40	2.80	13.30
Ce	10.40	10.20	10.10	15.10	168.00	59.20	12.60	7.40	10.7	4.90	33.70
Pr	1.61	1.67	2.44	2.10	20.78	6.21	1.77	1.20	1.90	0.83	6.03
Nd	6.40	8.30	12.20	9.30	83.20	23.70	7.50	6.40	8.60	3.90	27.50
Sm	1.57	2.12	3.64	2.14	13.54	4.59	1.60	1.80	2.44	1.11	6.00
Eu	0.55	0.79	1.39	0.76	3.61	1.28	0.49	0.50	0.91	0.33	1.65
Gd	1.83	2.67	5.06	2.43	8.62	4.33	1.63	1.88	3.04	1.52	5.23
Tb	0.33	0.55	0.98	0.45	0.90	0.68	0.25	0.33	0.63	0.30	0.83
Dy	2.09	3.39	6.16	2.92	4.14	3.64	1.43	1.78	3.97	1.83	4.09
Ho	0.50	0.78	1.43	0.59	0.64	0.71	0.28	0.36	0.81	0.44	0.79
Er	1.37	2.30	4.02	1.87	1.63	1.82	0.84	1.02	2.51	1.23	2.17
Tm	0.21	0.34	0.57	0.28	0.21	0.27	0.12	0.14	0.37	0.19	0.31
Yb	1.35	2.16	3.78	1.77	1.40	1.54	0.78	0.83	2.34	1.13	1.89

10

Table 1 (*continued*)

| | METAMAFIC | | | | | METAPLUTONIC | | | | | |
| | AMPHIBOLITE (ex) | | METATUFF (exh) | | DIKE (in) | ACTINOLITITE (in) | | | | | |
	SMSP30	VI-14B	SMSP109B	SMSP122J	SMSP23B	SMSP45	SMSP88A	VE-22B	VI-109A	VI-12C	VI-65A
Lu	0.22	0.33	0.57	0.30	0.19	0.21	0.12	0.12	0.34	0.17	0.27
Hf	1.30	1.70	2.60	1.90	8.90	1.20	0.80	0.90	1.80	0.80	2.20
Ta	0.10	0.20	0.20	0.30	0.40	0.10	0.10	0.10	0.20	0.10	0.70
Pb	0.20	2.00	0.10	0.80	3.10	0.80	4.40	0.30	2.10	1.90	1.10
Th	0.20	0.50	0.20	0.40	4.40	0.40	0.80	0.40	0.30	0.20	1.10
U	0.10	0.30	0.10	0.10	4.90	0.30	0.20	0.20	0.20	0.10	1.50
Be	1.00	1.00	1.00	1.00	3.00	1.00	2.00	1.00	1.00	1.00	6.00
Sc	34.00	48.00	44.00	27.00	16.00	46.00	20.00	74.00	44.00	57.00	59.00
ΣREE	71.23	94.3.0	107.44	77.61	423.96	180.38	65.11	103.26	93.56	81.78	175.36

and LREE contents, but with minor effect on Ta, Nb, Y, Ti and HREE contents.

The two metatuff samples are differentiated: one of the samples presents horizontal REE pattern, with REE enrichment around 10 times the chondrite values, and another exhibits a slight negative Ce anomaly and sub-horizontal MREE and HREE patterns. Both present low ΣREE contents (16.57–57.23 ppm), $(La/Yb)_N$ ratios (1.13–8.33) and weak positive Eu anomaly $[(Eu/Eu^*)_N = 0.64–2.66]$. Positive Rb and K and negative Ti anomalies are depicted in the multi-element diagram with chondrite-normalized trace elements (Thompson, 1982, Fig. 10E and F).

The metabasic dike presents strong LREE enrichment (La above 100 ppm) in relation to HREE (Lu below 0.20 ppm). The analyzed sample yields ΣREE = 383.26 ppm, $(La/Yb)_N$ ratio = 37.14 and Eu $[(Eu/Eu^*)_N = 1.02]$.

The plutonic mafic-ultramafic rocks exhibit slightly enriched sub-horizontal LREE pattern in relation to HREE. ΣREE contents fall between 20.68 and 130.58 ppm, $(La/Yb)_N$ ratios between 1.57 and 9.90, and a slightly negative to positive Eu anomaly $[(Eu/Eu^*)_N = 0.78–1.02]$ is observed. In the chondrite-normalized multi-elementary diagram by Thompson (1982), positive Ba, La, Ce, Nd, Sm, and Tb and negative Rb, Nd, P, Nb, and Ta anomalies and discrete Ti depletion are observed (Fig. 10G).

The observed LREE enrichment can be related to fractionation of ferromagnesian minerals rich in compatible elements and to enrichment of incompatible elements in the residual liquid.

The fairly similar chemical composition between actinolitites and magnesian schists, as well as their spatial distribution with the mafic-ultramafic metavolcanic rocks, allows one to suppose that some actinolitites could have been cumulates or sills cogenetic with the ultramafic floods strongly transformed by metasomatic processes.

6.2. Pre-collisional magmatism tectonic setting

Some geochemistry diagrams were also used in the study of the SPGB tectonic setting, particularly those that correlate trace elements considered immobile.

In the Th/Yb vs. Nb/Yb diagram by Pearce (2014) (Fig. 11A), the samples plot above the area not related to subduction, to N-MORB-OIB arrays, to zones richer in the Th/Yb ratio, in the island arc context, probably a back-arc-type basin, involving interaction of mantle rocks with crustal material.

Condie (2015), based on the immobile element ratios Zr/Nb vs. Nb/Th, established a relationship between the mafic-ultramafic rocks and the mantle sources. According to this author, the rocks originated from the depleted mantle present Nb/Th > 8 and Zr/Nb > 20; those from enriched mantle present high Nb/Th ratios, but exhibit Zr/Nb < 20. Moreover, those from the hydrated mantle, such as in subduction zones, yield very low Nb/Th ratios (< 8) and varied Zr/Nb ratios (Fig. 11B).

The magnesian schists yield Zr/Nb ratios between 6.79 and 22.89 and Nb/Th ratios between 3 and 12; the actinolitites yield Zr/Nb ratios between 4 and 29.33 and Nb/Th ratios between 2.25 and 13.18, and the amphibolites yield Zr/Nb ratios between 17.75 and 24.95 and Nb/Th ratios between 1.58 and 13.50. The majority of the samples concentrate in the hydrated mantle field and the others in the enriched mantle field, associated with deeper mantle melting.

In the V vs. Ti diagram by Shervais (1982) (Fig. 11C), the rocks of this study concentrate in the field of the back-arc (BABB) or fore-arc (FAB) basic rocks or island-arc tholeiites.

The komatiites basaltic, in turn, represent magmas formed in high-temperature conditions (~1600 °C), with their origin being attributed to two formation processes (Arndt, 2008): i. mantle plumes developed in both intra-oceanic plateaus and continental crust; ii. hydric melting of the mantle wedge overlying the subduction zone. However, the majority of the authors consider that the komatiites come from mantle plumes and that different types of komatiites or basaltic komatiites
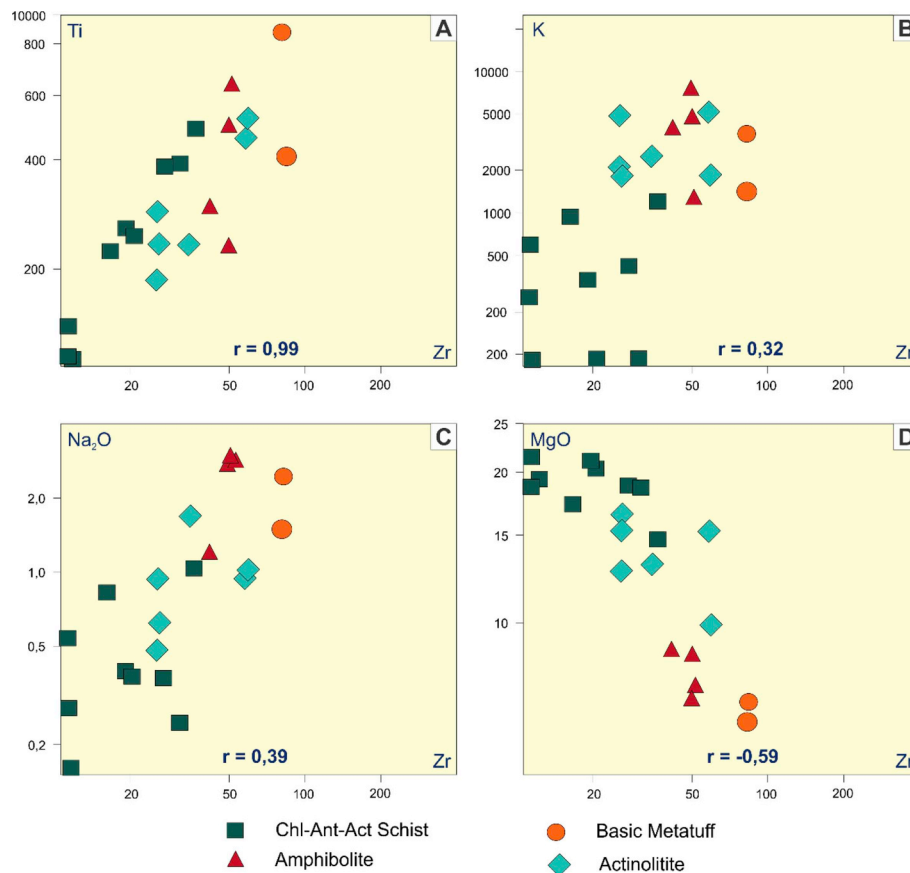
Fig. 7. A. Perceptible trend for the immobile elements in the Zr vs. Ti diagram, with best confidence level. B. Strong alteration and mobility indicated in the Zr vs. K diagram (Polat and Hofmann, 2003). C. Zr vs. Na2O diagram. D. Zr vs. MgO diagram.

reflect the composition of the mantle source and the partial melting degree in different parts of the mantle plume.

The tholeiitic basalts develop in several contexts: convergent plate margin settings of the island-arc and continental margin types; divergent plate settings of the mid-oceanic ridge and back-arc basin types; and intraplate settings of the ocean-island and continental rift types.

In the diagram Nb-Zr-Y by Meschede (1986) (Fig. 11D), used to discriminate basic or basic-intermediate volcanic settings, excepting for the metabasic dike, the magnesian schists, the amphibolites and basic metatuffs are distributed in the volcanic-arc (VAC) fields.

As it was seen before, SPGB is characterized by a magmatic association that reflects a bimodal magmatism characteristic of an extensional setting. The magnesian schists, metamorphism products of komatiitic basalts types reflect an extensional setting in the island arc context, probably in a back-arc-type basin.

The amphibolites originated of tholeiitic basalts also present a mantle source, probably shallower and more fractionated than that of the ultramafic schists. The low $(La/Yb)_{CH}$ ratios (0.74–3.82) and negative Nb, Ta and Ti anomalies of these rocks indicate interaction between mantle and crustal rocks compatible with magmatic associations developed in extensional setting in a volcanic arc context (Fig. 11D).

The presence of this magmatic association intercalated within arkosic gneiss, acid metavolcanic rocks and aluminous schists suggests the existence of an older thin continental crust that rifted and evolved for the development of a proto-oceanic crust. The occurrence of metaexhalites (tourmalinites, gondites and metacherts), intercalated with amphibolitized volcanic rocks and the magnesian schists indicates that their formation represent extrusion activity.

Thus, the geologic and chemical datasets indicate that the rocks of ultramafic and mafic oceanic nature, affinity T-MORB or N-MORB and VAB (Fig. 11D) developed in an extensional setting, submerged rift or a back-arc-type basin, with the development of an incipient oceanic crust.

Applying La/Sm Vs. Nb/Th and La/Sm vs. La/Ta according to Said et al. (2012), the samples plot in the fields E-HMT, E-HMT2, KB, E-KB2 and E-KB1 (Fig. 12A). Therefore, we have mostly typical lithotypes enriched in magnesium and potassium indicating that the volcanism and some plutonic rocks of the TTG sequence had crustal contamination during the subduction process. In contrast, some samples do not present this contamination and are shown to be free of change (UC – Uncontaminated Crust) (Fig. 12B).

7. Geochronology

Five rocks of SPGB were analyzed using the zircon U-Pb method – metapelitic (1 sample), meta-acid intrusive (3 samples), and metagranitic (1 sample), and ten metaultramafic, meta-acid, metavolcaniclastic, meta-intrusive and metagranitic rock samples were analyzed by the whole-rock Sm-Nd method (Fig. 3).

The SPGB rock types yield Paleoproterozoic zircon U-Pb ages between 2.2 and 2.1 Ga. **The garnet-kyanite schists** exhibit 2207 ± 14 Ma (Rhyacian) ages (Fig. 13A). This schist formed from sedimentation triggered by the reworking of volcanic rock associations that crystallized around the volcanic arc, precursor and/or synchronous to its opening.

The three samples of **metadacites** yield ages of 2234 ± 13 Ma (Fig. 13B), 2212 ± 13 Ma (Fig. 13C) and 2156 ± 45 Ma (Fig. 13D), compatible with the Rhyacian volcanism. The first two are located on the western and eastern borders of the basin, respectively. As they yield similar ages and compositions and correspond to the bottom of the basin, they can be interpreted as crystallization ages of the first meta-acid flows. The third sample, located in the central portion, is interpreted as a later acid volcanism event. The volcanism seems to precede
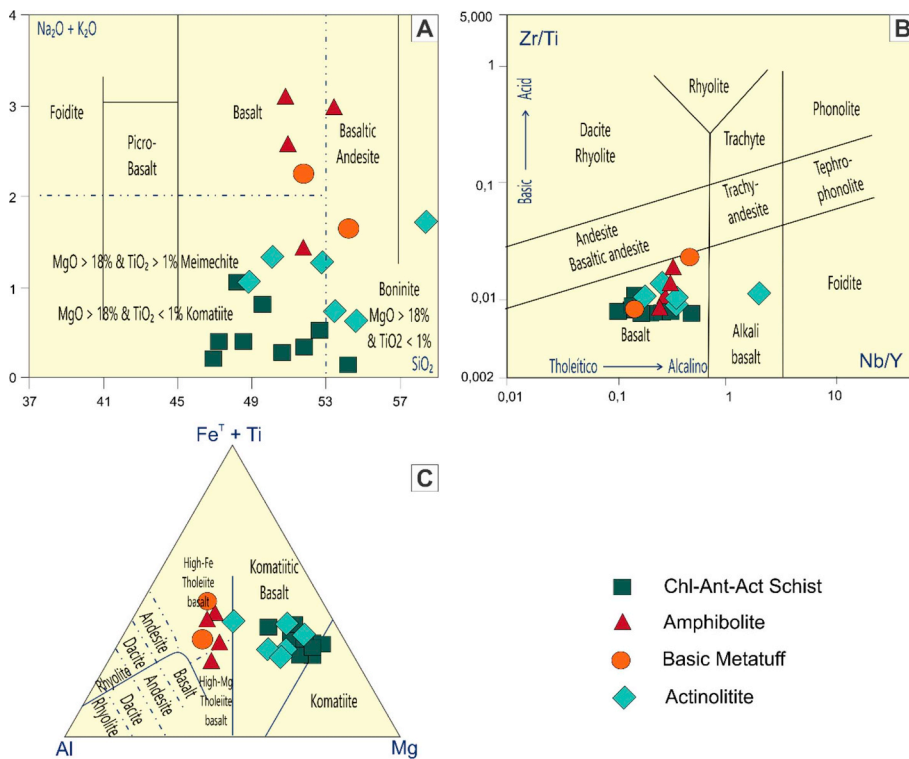
Fig. 8. A. TAS diagram of Le Bas (2000) for the SPGB mafic-ultramafic association. B. Zr/Ti vs. Nb/Y diagram of Pearce (2014) for the SPGB mafic-ultramafic samples. C. Cationic diagram by Jensen (1976) for the classification of mafic and ultramafic rocks, with concentration of metaultramafic and plutonic rocks in the komatiitic basalts field, of metamafic rocks in the Fe- and Mg-rich tholeiite field, and the metamafic dike in the transitional field.

or be concomitant with the ultramafic volcanic activity, for the magnesian schists dated by Liégeois (in Arthaud et al., 2008) yield 2.06 ± 0.1 Ga (Sm-Nd) in the Madalena region (State of Ceará).

The **metabasic dike** that discordantly crosscuts the Rhyacian tectonic banding of the mafic-ultramafic metavolcanic and metadacitic rocks and metatuffs yields a (U-Pb) age of 2194 ± 8.3 Ma are interpreted inherited zircons (Fig. 13E).

The **metagranodiorite** represents the TTG sequence, with U-Pb crystallization age of 2181 ± 4.4 Ma (Fig. 13F), This fact also places it in the Upper Rhyacian synchronic with the volcano-sedimentary sequence.

The results obtained from the Sm-Nd analysis are heterogeneous, demonstrating that the isotopic system was opened during the Brasiliano Cycle (Dantas et al., 2002).

Fortunately, the Sm-Nd system preserves the original isotopic characteristics of the mantle-crust differentiation process, during crust evolution or alteration (Pimentel and Silva, 2003), even if the rocks underwent isotopic fractionation as a result, for example, of metamorphism, in special of high grade (Ben Othman et al., 1984; Burton and O'Nions, 1992; Oliveira et al., 2002; Tassinari et al., 2004; Carneiro et al., 2004; Barbosa et al., 2013).

The analyses were performed in terms of the $^{147}Sm/^{144}Nd$ and $^{143}Nd/^{144}Nd$ ratios and the ε_{Nd} notation (Table 2). The initial ratios were recalculated according to the zircon U-Pb ages of 2.21 Ga for the metadacite and 2.18 Ga for the metagranodiorite. The age of 2.06 Ga obtained by Liégeois (in Arthaud et al., 2008) for the **SPGB** magnesian schists was adopted for the chlorite-anthophyllite-actinolite/tremolite schist and basic metatuff.
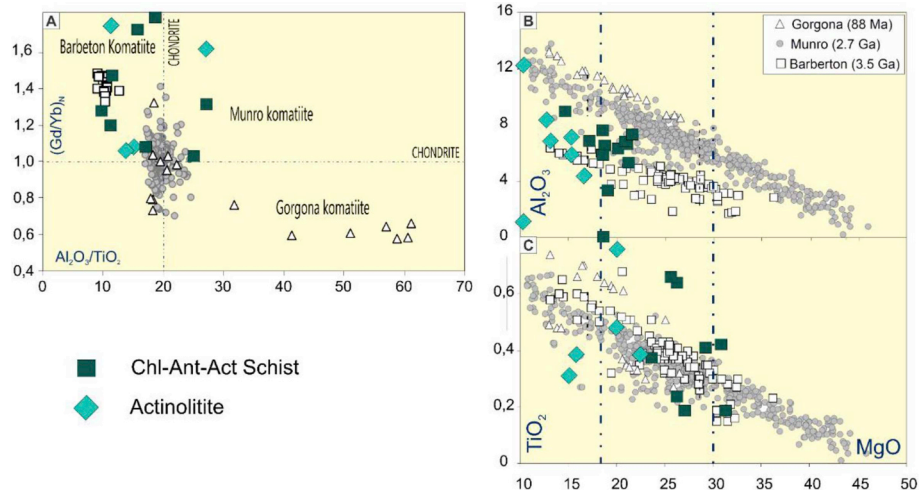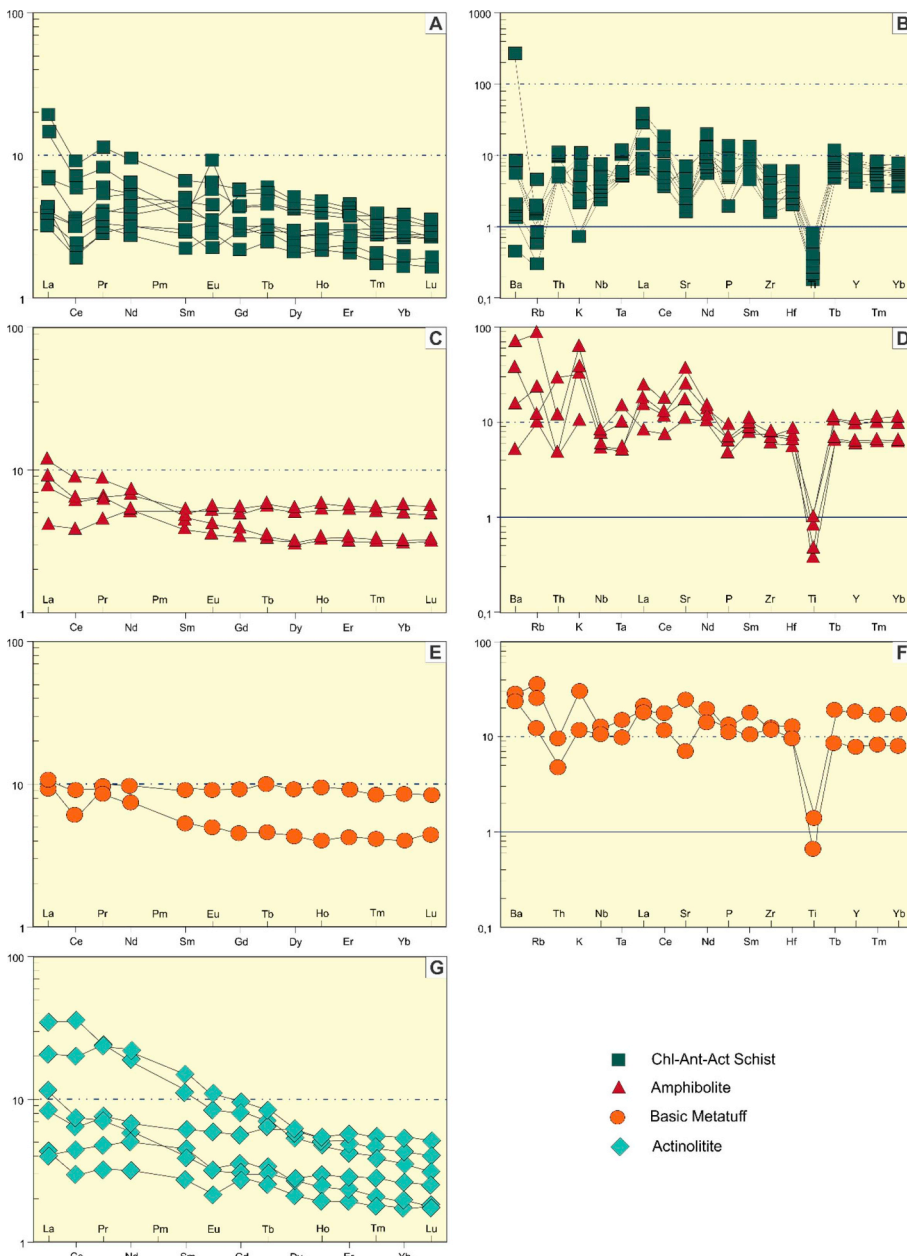

Fig. 9. A. Al2O3/TiO2 vs. (Gd/Yb)N, B. MgO vs. Al2O3 and C. MgO vs. Al2O3 diagrams comparing three komatiitic types with magnesian schists of SPGB. The plotting is attributed to the transitional zones between the Munro and Barberton types.

Fig. 10. A. Chondrite-normalized REE diagrams for the SPGB metaultramafic group (McDonough and Sun, 1995). B. Chondrite-normalized multi-element diagram (Thompson, 1982). C. Spidergrams for the SPGB metaultramafic group (chondrite values after McDonough and Sun, 1995). D. Multi-element diagram with chondrite-normalized trace elements (Thompson, 1982). E. Spidergrams for the SPGB metavolcaniclastic group (chondrite values after McDonough and Sun, 1995). F. Multi-element diagram with chondrite-normalized trace elements (Thompson, 1982). G. Spidergrams for the actinolitite of the SPGB hydrous meta-intrusive group (chondrite values after McDonough and Sun, 1995).

In the $^{143}Nd/^{144}Nd$ vs. $^{147}Sm/^{144}Nd$ diagram (Fig. 14) a trend defined by metagranite, metadacite and metavolcaniclastic rocks and a metaultramafic sample can be observed, which demonstrates that there was no isotopic scattering and a higher confidence can be assumed for this lithologic group. The mafic and ultramafic rocks higher scattering (Fig. 14) reflecting a more evident metasomatism due to the lower abundance of Sm and Nd in these rocks.

The other metaultramafic samples yielded discrepant values, which suggests a distinct evolution or perturbations resulting of the Brasiliano metamorphism in the basic rocks, opening the isotope system and producing different and unreliable TDM ages.

In the isotopic evolution diagram (Fig. 15), the results produced T_{DM} ages that demonstrated Archean to juvenile sources, but with significant errors regarding the magnesian schists and the metabasic dike, because they plot above the depleted mantle line.

The **SPGB** magnesian schists present probably (3.39 Ga) as described in this research. Other authors such as Fetter (1999) and Costa et al. (2018), the latter using the Lu-Hf (zircon) method, obtained ages between 3.04 and 2.69Ga and 2.8 to 2.6Ga for metatonalites, respectively.

The acid volcanism (metadacite, metagranodiorite and metatuff) is less affected with respect to the SM/ND system. Its TDM values are closer to the ages obtained in the zircons that have crystallization ages between 2.36 Ga to 2.07 Ga.

The **TTG**-type plutonism is represented by the metagranodiorite, with mafic enclaves. It yields a T_{DM} age of 2.36 Ga, being inferred as resulting from crustal melting. Other paleoproterozoic TTG occurs in the nucleus or its border, Arthaud (2007), Martins et al., (2009) confirming the infracrustal plutonism.

Acid volcanism shows $\varepsilon nd(0)$ values ranging from -11 to -25, denoting rocks derived from crustal sources. The basic rocks, even with open Sm-Nd system, show a variation in the εnd values always close to -5 to $+5$ (Fig. 15), thus, juvenile sources could be inferred for this group. This reflects crustal rejuvenation and the participation of the mantle in the formation of magnesian schists and actinolitites, probably during the volcanosedimentary process.

The sequence is hosted/limited by the Archean Nucleus (Cruzeta Complex), which rock types are strongly deformed and migmatized. Dating performed by Fetter (1999) applying the zircon U-Pb method to

14
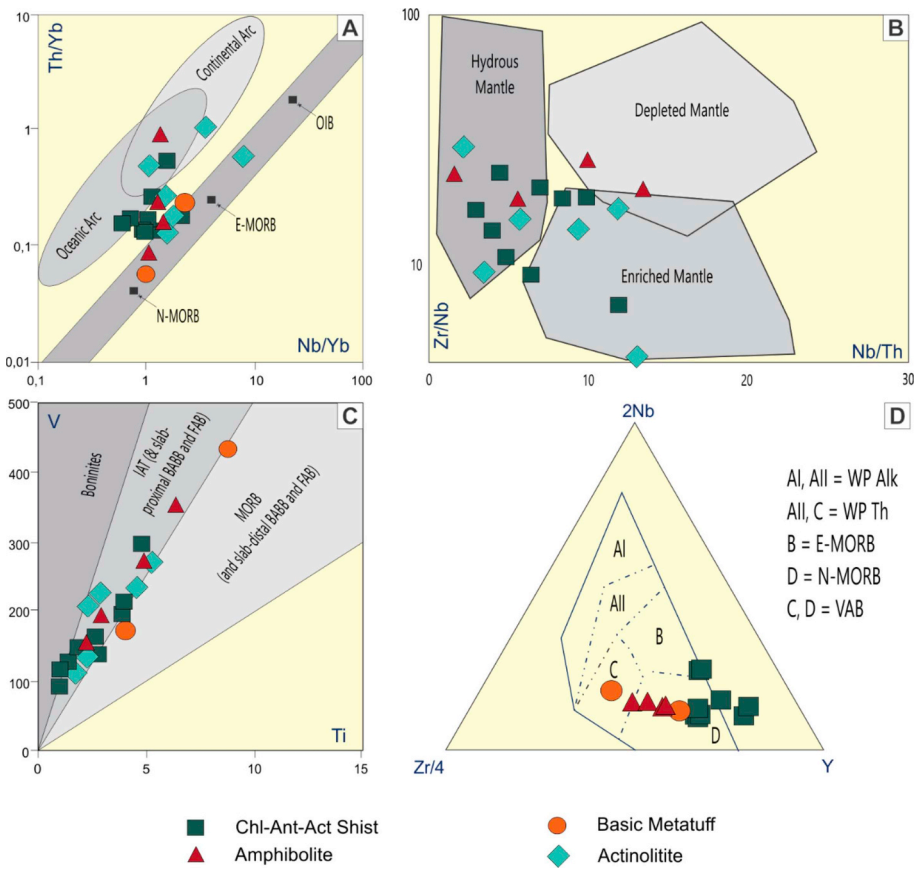
Fig. 11. A. Th/Yb vs. Nb/Yb (Pearce, 2014) and B. TiO₂/Yb vs. Nb/Yb (Pearce, 1998) diagrams for the samples of this study, attesting the island arc context. B. Nb/Th vs. Zr/Nb diagram identifying the mantle sources for the SPGB metamafic-ultramafic rocks (Condie, 2015). C. Ti vs. V diagram (Shervais, 1982) attesting the back-arc (BABB), fore-arc (FAB) or island-arc tholeiite contexts for the rocks of the study area. D. The Meschede (1986) diagram indicates the distribution of the metamafic-ultramafic rocks in the fields N-MORB and VAB.

metatonalites, resulted in ages between 2773 ± 60 Ma and 2857 ± 42 Ma, confirming their Archean age; and 2776 ± 65 Ma for the metatonalite. Silva et al. (2002) obtained a U-Pb age of 3270 ± 5 Ma for metatonalites of the complex, confirming the Archean age of the Cruzeta Complex.

The Brasiliano event described in several lower intercepts of concordia lines presented ages between 637 ± 110 and 406 ± 74 Ma, reflecting the Neoproterozoic collage event. Several shear zones developed, as well as Neoproterozoic terranes being amalgamated to SPGB. Despite the recording of this orogeny in the study area, it did not obliterate the Paleoproterozoic history.

8. Geotectonic evolution

The geologic, petrographic, geochemical and geochronological dataset obtained in this study confirms several volcanic and plutonic events in SPGB during the Paleoproterozoic.

The first stage (Fig. 16A) would be associated with the generation of infracrustal magmas that between 2.2 and 2.1 Ga originated the TTG-type plutonic magmatic arcs on the border and intruded into the Archean Nucleus (Cruzeta Complex). The TTG rocks present mineralization typical of a porphyry copper system, yielding ages around 2156 Ma (Castro, 2004).

During the initial stage of the extensional basin, psammitic-pelitic-marly sediments deposited. The still thin crust undergoing extension, as a result of the taphrogenesis that was taking place, allowed the rise of mantle material. Magmas of komatiitic basalts and tholeiitic characteristics ascended through the fissures generated during the taphrogenesis, leading to concomitant flows and intrusions. Flows of acid and basic pyroclastic magmas occur in similar and synchronic way to this mafic-ultramafic association, as recorded by their frequent intercalations in this magmatic group. With the end of the bimodal volcanism, several exhalites were deposited, including chert, gondites, banded iron formations and tourmalinites in subaqueous setting.
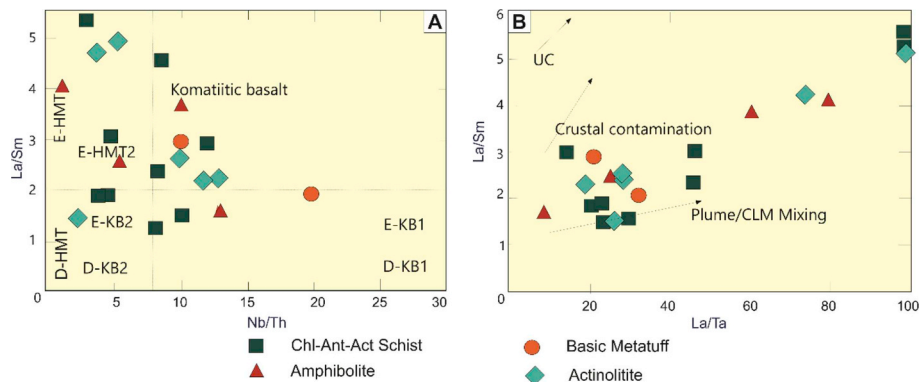
Fig. 12. A. (La/Sm)n vs. Nb/Th diagram after Said et al. (2012). B. (La/Sm) vs. (La/Ta) illustrating the different trends (arrows) for contamination of plume liquids by continental lithospheric mantle (CLM).
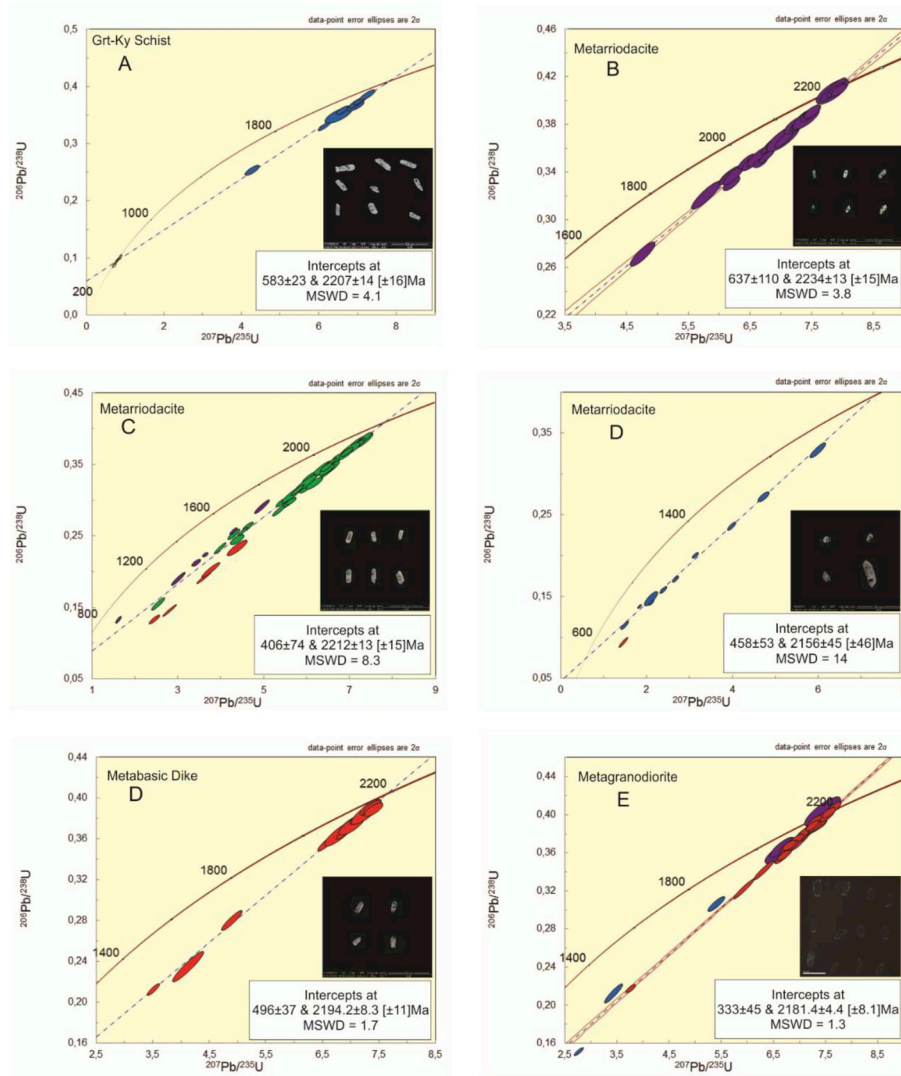
Fig. 13. Concordia diagram for the SPGB samples analyzed by the zircon U-Pb method, metasediment (A), metavolcanic (B, C and D), metabasic dike (E) and metagranodiorite (F).

Table 2

Sm-Nd isotopic compositions of the SPGB groups.

SAMPLE	GROUP	Sm	Nd	^{147}Sm	^{143}Nd	2σ	ε Nd 0	ε Nd t	TDm (Ga)
				^{144}Nd	^{144}Nd				
CVP06 Chl-Ant-Act/Tr Schist	METAULTRAMAFIC	1.38	4.36	0.1911	0.512576	± 0.000001	−1.21	0.22	3.39
CVP03 Chl-Ant-Act/Tr Schist		2.87	11.5	0.1509	0.512428	± 0.000009	−4.1	7.75	1.49
CVP02 Chl-Ant-Act/Tr Schist		2.58	7.18	0.2176	0.513104	± 0.000017	9.09	3.73	1.01
CVP01 Chl-Ant-Act/Tr Schist		2.51	8.41	0.1805	0.512944	± 0.000014	5.97	10.19	0.51
SMSP04 Meta-granodiorite	METAMAFIC	3.93	21.41	0.1109	0.511456	± 0.000003	−23.06	0.98	2.36
CVP05 Basic Metatuff		2.03	8.33	0.147	0.512058	± 0.000004	−11.31	1.49	2.26
SMSP23B Metabasic Dike		19.24	114.24	0.1019	0.511783	± 0.000010	−16.68	10.12	1.71
SMSP23A Metadacite	META ACIDE	4.27	20.07	0.1287	0.511796	± 0.000004	−16.42	2.91	2.24
SMSP75 Metadacite		5.5	29.94	0.1111	0.511606	± 0.000011	−20.13	4.46	2.14
CVP04		0.74	5.11	0.0871	0.511325	± 0.000024	−25.61	4.78	2.07

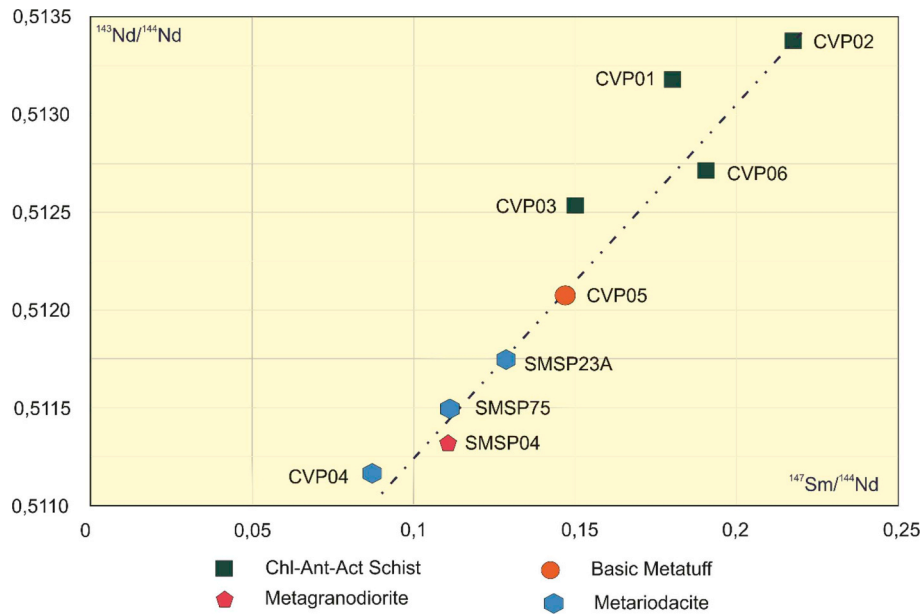**Fig. 14.** $^{143}Nd/^{144}Nd$ vs. $^{147}Sm/^{144}Nd$ diagram, showing that there is an isotopic scatter of the analyses, attesting that they are aligned and cogenetic.

The second stage (Fig. 16B) is represented by subvolcanic basic dikes that cut the metavolcanosedimentary sequence and the granitic rocks preceding, indicates that the extensional processes still persisted in the basin at the 1.7Ga.

The third stage (Fig. 16C) occurs after the taphrogenic processes. It is characterized by the closing of the basin in the Brasiliano cycle, which deformed the rock types in different steps or phases to the amphibolite facies. The beginning was marked by a low-angle tectonism, causing the transposition of primary planar fabrics and the layer repetition by thrusting and tight folding, ending with the development of shear zones imprinted in different rock types. The possible obliteration of the primary textures characteristics of the mafic-ultramafic (meta) volcanic rocks, such as spinifex and pillow lavas, can have occurred during these tectonometamorphic events.

9. Conclusions

Lithostratigraphically the study area is composed of metasedimentary psammitic-pelitic-marly rocks, metamafic-ultramafic volcanic and meta-acid flows, intercalated with basic and acid metatuffs, meta-exhalites and hydrothermally altered rocks. The rock types are crosscut by Paleoproterozoic metamafic-ultramafic intrusions, metagranodiorites, a metabasic dike and later by Neoproterozoic granitoids. The occurrence of meta-exhalites (tourmalinites, gondites and metacherts) intercalated with amphibolitized volcanic rocks and magnesian schists indicates that they formed in a subaqueous rift setting.

Deformation started during the Orosirian and was later resumed in the Brasiliano, imprinting a NE-SW-trend and causing the transposition of primary planar fabrics and layer repetition by thrusting and tight
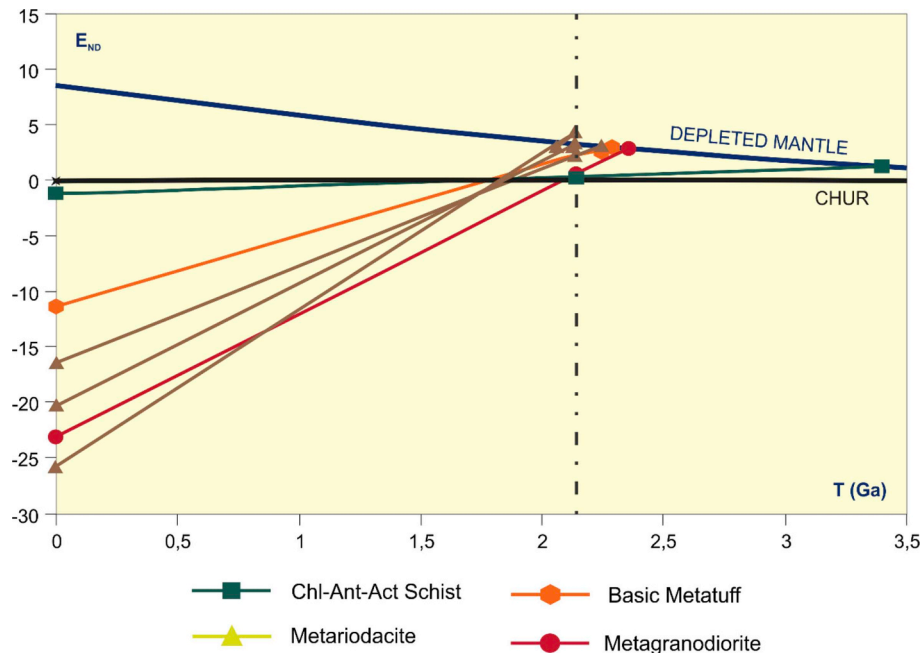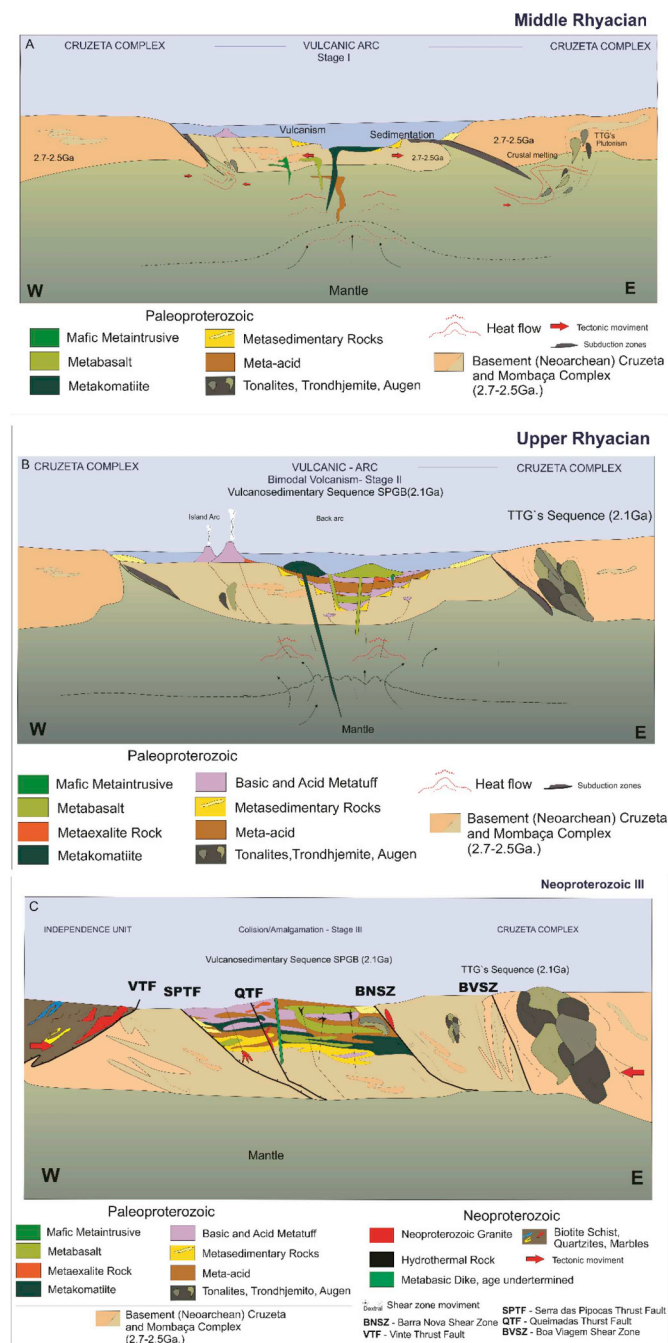

Fig. 15. Isotopic evolutionary diagram T(Ga) vs. ε_{Nd} for the SPGB analyzed samples.

Fig. 16. Tectonic evolution of Serra das Pipocas Greenstone Belt between Middle Rhyacian (A), Upper Rhyacian (B) and Neoproterozoic III (C).

folding. Hydrothermal alteration caused chemical changes in the protolith original compositions, which requires caution when treating the geochemical data. For a better analysis of the data, immobile major and trace elements were used in most of the diagrams.

The magnesian schists although not presenting typical textural characteristics of komatiitic rocks, such as the spinifex texture and polyhedral joints, occur in layers separated by basic metatuffs, which suggests that they were originally volcanic flows. The geochemical data indicate as its protoliths komatiitic basalts, revealing features between komatiites of Munro and Barberton types.

The mafic rock types were classified as high iron and magnesium tholeiitic basalts. Both magmatic events occurred in an extensional setting of magmatic arcs or oceanic plateaus associated with mantle plumes. The chemical composition of some mafic-ultramafic

metaplutonic rocks is similar to that of the flows, which suggests that they corresponded to cumulates or cogenetic sills originated from the mantle sources in question.

The lithologic association was developed in submerged extensional intracontinental setting, in an island-arc context, probably in a back-arc-type basin. During the taphrogenesis the first psammitic-pelitic-marly and pyroclastic sediments were deposited, mantle materials ascended and plutonism occurred synchronically. With the end of the bimodal volcanism, exhalites were deposited in a subaqueous setting. Subvolcanic basic dikes associated with late Rhyacian granodioritic intrusions indicate that the extensional processes still persisted in the basin for several thousand years. The granodioritic intrusions were accompanied by hydrothermal fluids that may have triggered sulfide mineralization together with volcanism (lavas and pyroclastic rocks) and pelagic sedimentation. To better understand this sulfide mineralization, a detailed study of the 500 m-wide hydrothermally altered zone that stretches out for approximately 16 km in the NE-SW direction is necessary.

Acknowledgements

Appendix A. Supplementary data

Supplementary data to this article can be found online at https://doi.org/10.1016/j.jsames.2019.102220.

References

Albano, D.M., Sousa, R.D., 2005. Aspectos Geológicos, Petrográficos e Estruturais da Sequência Metavulcanossedimentar de Cruzeta Adjacências Área II. Monografia. Departamento de Geologia. Universidade Federal do Ceará.

Almeida, F.F.M., Hasui, Y., Brito Neves, B.B., Fuck, H.A., 1981. Brazilian structural provinces: an introduction. Earth Sci. Rev. 17, 1–29.

Almeida, F.F.M., Hasui, Y., Brito Neves, B.B., Fuck, R.A., 1977. Províncias estruturais brasileiras. In: SBG/Núcleo Nordeste, Simp. Geol. NE, vol. 8. Campina Grande, Atas, pp. 363–391.

Amaral, W.S., 2010. Análise geoquímica, geocronológica e termobarométrica das rochas de alto grau metamórfico, adjacentes ao arco magmático de Santa Quitéria, NW da Província Borborema. Tese de Doutorado. Universidade Estadual de Campinas-UNICAMP.

Araújo, C.E.G., Basei, M.A.S., Grandjean, F.C., Armstrong, R., Brito, R.S., 2017. Contrasting Archaean (2.85–2.68 Ga) TTGs from the Tróia Massif (NE-Brazil) and their geodynamic implications for flat to steep subduction transition. Precambrian Res. 297, 1–18.

Arndt, N., 2008. Komatiite, first ed. Cambridge University Press, New York.

Arthaud, M.H., Landim, D.F., 1995. Relações da Sequência Metassedimentar de Quixeramobim com seu embasamento. In: 16° Simpósio de Geologia do Nordeste, vol. 1. pp. 125–128.

Arthaud, M.H., 2007. Evolução Neoproterozoica do Grupo Ceará (Domínio Ceará Central, NE Brasil): da sedimentação à colisão continental brasiliana. Tese de Doutorado. Instituto de Geociências, Universidade de Brasília.

Arthaud, M.H., Caby, R., Fuck, R.A., Dantas, E.L., Parente, C.V., 2008. Geology of the Northern Borborema Province NE Brazil and its Correlation with Nigeria, vol. 294. Geological Society, London, Special Publications, NW Africa, pp. 49–67.

Arthaud, M.H., Fuck, R.A., Dantas, E.L., Santos, T.J.S., Caby, R., Armstrong, R., 2015. The neoproterozoic Ceará group, Ceará central domain, NE Brazil: depositional age and provenance of detrital material. New insights from U-Pb and Sm-Nd, geochronology. J. South Am. Earth Sci. 58, 223.

Barbuena, D., 2017. Geochemistry and Geochronology of the Supracrustal Rocks of the Mundo Novo Greenstone Belt, Bahia: Evidences of a Back-Arc Basin in the Transition between the Meso-And Neoarchean. 2017. 1 Recurso Online. Tese (doutorado). Universidade Estadual de Campinas, Instituto de Geociências, Campinas, SP, pp. 174.

Baratoux, L., Metelka, V., Naba, S., Jessel, M.W., Grégoire, M., Ganne, J., 2011. Juvenile Paleoproterozoic crust evolution during the Eburnean orogeny (~2.2e2.0 Ga), western Burkina Faso. Precambrian Res. 191 (1e2), 18e45.

Barbosa, N.S., Teixeira, W., Leal, L.R.B., Leal, A.B.M., 2013. Evolução crustal do setor ocidental do Bloco Arqueano Gavião, Cráton do São Francisco, com base em evidências U-Pb, Sm-Nd e Rb-Sr. Geol. USP, Série científica, São Paulo 13 (4), 6–88.

Ben Othman, D., Polve, M., All&e, C.J., 1984. Nd-Sr isotopic composition of granulites and constraints on the evolution of the lower continental crust. Nature 307, 510–515.

Brito Neves, B.B., Santos, E.J., Van Schmus, W.R., 2000. Tectonic history of the Borborema Province. In: Cordani, U.G., Milani, E.J., Thomaz Filho, A., Campos, D.A. (Eds.), Tectonic Evolution of the South America. 31st International Geological Congress, 2000, pp. 151–182 Rio de Janeiro, Brasil.

Brito Neves, B. B. de, 1975a. Regionalização Geotectônica Do Pré-Cambriano Nordestino. São Paulo. Tese de Doutorado. Instituto de Geociências, Univer sidade de São Paulo, Tese de Livre Docência 198p.

Brito Neves, B.B., 1975b. Regionalização Geotectônica Do Pré–Cambriano Nordestino (Ph.D. thesis). Universidade de São Paulo, São Paulo–SP, pp. 198.

Buhn, B., Pimentel, M.M., Matteini, M., Dantas, E.L., 2009. High spatial resolution analysis of Pb and U isotopes for geochronology by laser ablation multi-collector inductively coupled plasma mass spectrometry (LA-MC-ICP-MS). Anais da Acad. Bras. de Ciências 1, 1–16.

Burton, K.W., O'Nions, R.K., 1992. The timing of mineral growth across a regional metamorphic sequence. Nature (London) 357, 235–238.

Caby, R., Arthaud, M.H., 1986. Major precambrian nappes of the Brazilian belt, Ceará, northeast Brazil. Geology 14, 871–874.

Caby, R., 1989. Precambrian terranes of Benin-Nigeria and northeast Brazil and the late proterozoic South atlantic fit. In: In: Fallmeyer, D.D. (Ed.), Terranes in the Circum-Atlantic Proterozoic Orogens, vol. 230. Geological Society of America, Special Papers, pp. 145–158.

Caby, R., Arthaud, H.H., Archanjo, C.J., 1995. Lithostratigraphy and petrostructural characterization of supracrustal units in the Brasiliano Belt of northeast Brazil: geodynamic implication. J.S. Am. Earth Sci. 8, 235–246.

Carneiro, M.A., Teixeira, W., Carvalho Jr., I.M., Pimentel, M.M., Oliveira, A.H., 2004. Comportamento dos Sistemas Sm-Nd e Rb-Sr da Sequência Acamadada Máfico-Ultramáfica Ribeirão dos Motas (Arqueano), Cráton São Francisco Meridional: evidências de enriquecimento mantélico e fracionamento isotópico. Revista do Instituto de Geociências, USP 2 (4), 13–26.

Castro, N.A., 2004. Evolução Geológica Proterozoica da região entre Madalena e Taperuaba, Domínio Tectônico Ceará Central (Província Borborema). Tese de Doutorado. Universidade de São Paulo.

Cavalcante, J.C., 1999. Limites e evolução do Sistema Jaguaribeano, Província Borborema, Nordeste do Brasil. Dissertação de mestrado. Universidade Federal do Rio Grande do Norte Natal 183pp.

Cavalcante, J.C., Vasconcelos, A.M., Medeiros, M.F., Paiva, I.P., Gomes, F.E.M., Cavalcante, S.N., Cavalcante, J.E., Melo, A.C.R., Duarte Neto, V.C., Benevides, H.C., 2003. Mapa Geológico Do Estado Do Ceará – Escala 1:500.000. Fortaleza, Ministério das Minas e Energia/Companhia de Pesquisa de Recursos Minerais.

Condie, K., 2015. Changing tectonic setting through time: indiscriminate use of Geochemical discriminant diagrams. Precambrian Res. 226, 587–591.

Costa, F.G., Oliveira, E.P., McNaughton, N., 2011. The Fazenda Gavião granodiorite and associated potassic plutons as evidence for Palaeoproterozoic arc-continent collision in the Rio Itapicuru greenstone belt, Brazil. J. South Am. Earth Sci. 32 (2), 127–141.

Costa, F.G.C., Palheta, E.S.M., Rodrigues, J.B., Gomes, I.P., Vasconcelos, A.M., 2015. Geochemistry and U&Pb zircon ages of plutonic rocks from the Algodões granite-greenstone terrane, Troia Massif, northern Borborema Province, Brazil: implications for Paleoproterozoic subduction-accretion processes. J. South Am. Earth Sci. 59, 45e68 (2015).

Costa, Felipe Grandjean, Klein, Evandro, Lafon, Jean-Michel, Milhomem Neto, João, Galarza, Marco, Rodrigues, Joseneusa, Naleto, João, Lima, Rafael, 2018. Geochemistry and U–Pb–Hf zircon data for plutonic rocks of the Troia Massif, Borborema Province, NE Brazil: evidence for reworking of Archean and juvenile Paleoproterozoic crust during Rhyacian accretionary and collisional tectonics. Precambrian Res. 311. https://doi.org/10.1016/j.precamres.2018.04.008.

Dantas, E.L., 2009. O Greenstone Belt de Serra Caiada: Evidências de antiga crosta oceânica no Maciço São José do Campestre-RN. In: Simpósio de Geologia do Nordeste, Fortaleza. CD-ROM, Brasil.

Dantas, E.L., Hackspacher, P.C., Magini, C., Legrand, J.M., 2002. Sistema Sm-Nd em rocha-total aberto versus fechado: comportamento isotópico em zonas de alta deformação. Geologia USP. Série Científica, São Paulo 2, 109–129.

De Wit, M.J., Brito Neves, B.B., Trouw, R.A.J., Pankhurst, R.J., 2008. Pre-Cenozoic correlations across the South Atlantic region: "the ties that bind". In: In: Pankhurst, R.J., Trouw, R.A.J., Brito Neves, B.B., De Wit, M.J. (Eds.), West Gondwana: Pre-cenozoic Correlations across the Atlantic Region, vol. 294. Geological Society, London, special Publications, pp. 1–8.

Delgado, I. de M., et al., 2003. Geotectônica do Escudo atlântico. In: Bizzi, L.A., Schobbenhaus, C., Vidotti, R.M., Gonçalves, J.H. (Eds.), Geologia, Tectonica e Recursos Minerais do Brasil. Ministério de Minas e Energias. Serviço Geológico do Brasil – CPRM.

Fetter, A.H., 1999. U/Pb and Sm/Nd Geochronological Constraints on the Crustal Framework and Geological History of Ceará State, NW Borborema Province, NE Brazil: Implications Goes the Assembly of Gondwana. Thesis de Doutoramento. University of Kansas, pp. 164.

Fetter, A.H., Santos, T.J.S., Van Schmus, W.R., Hackspacher, P.C., Brito Neves, B.B., Arthaud, M.H., Nogueira Neto, J.A., Wernick, E., 2003. Evidence for neoproterozoic continental arc magmatism in the Santa Quitéria batholith of Ceará state, NW Borborema Province, NE Brazil: implications for assembly of west Gondwana. Gondwana Res. 6, 265–273.

Ganade, Carlos E., Basei, Miguel A.S., Grandjean, Felipe Costa, Armstrong, Richard, Brito, Reinaldo S., 2017. Contrasting Archaean (2.85?2.68 Ga) TTGs from the Troia Massif (NE-Brazil) and their geodynamic implications for flat to steep subduction transition. Precambrian Res. 297, 1–18 2017.

Ganade, Carlos E., Cordani, Umberto G., Agbossoumounde, Yao, Caby, Renaud, Basei,

Miguel A.S., Weinberg, Roberto F., Sato, Kei, 2016. NE Brazil and NW Africa connections: new U-Pb/Lu-Hf zircon data of a complete plate tectonic cycle in the Dahomey belt of the West Gondwana Orogen in Togo and Benin. Precambrian Res. 276, 24–42 Tightening-up.

Gioia, S.M.L.C., Pimentel, M.M., 2000. The Sm-Nd method in the geochronology laboratory of the University of Brasilia. An Acad. Bras Ciências 72, 2.

Janoušek, Vojtěch, Vrána, Stanislav, Erban, Vojtěch, Vokurka, Karel, Milan, Drábek, 2008. Metabasic rocks in the Varied Group of the Moldanubian Zone, southern Bohemia - their petrology, geochemical character and possible petrogenesis. J. Geosci. 53 (1), 31–64 2008.

Jensen, L.S., 1976. A New Cation Plot for Classifying Sub-alkaline Volcanic Rocks. Ontario Division Mines Miscellaneous. pp. 22 Paper No. 66.

Klein, E.L., Luzardo, R., Moura, C.A.V., Armstrong, R., 2008. Geochemistry and zircon geochronology of paleoproterozoic granitoids: further evidence on the magmatic and crustal evolution of the São Luis cratonic fragment. Brazil. Precambrian Res. 165 (3e4), 221e242.

Klein, E.L., Moura, C.A.V., Pinheiro, B.L.S., 2005. Paleoproterozoic crustal evolution of the São Luis craton, Brazil: evidence from zircon geochronology and Sm-Nd isotopes. Gondwana Res. 8 (2), 177e186.

Kock, G.S., Armstrong, R.A., Siegfried, H.P., Thomas, E., 2011. Geochronology of the Birim Supergroup of the West African craton in the Wa-Bolé region of westcentral Ghana: implications for the stratigraphic framework. Precambrian Res. 59 (1), 1e40.

Le Bas, M.J., 2000. IUGS reclassification of the high-Mg and picritic volcanic rocks. J. Petrol. 41 (10), 1467–1470.

Martins, G., Oliveira, E.P., Lafon, J.M., 2009. The Algodões amphibolite–tonalite gneiss sequence, Borborema Province, NE Brazil: geochemical and geochronological evidence for Palaeoproterozoic accretion of oceanic plateau/back-arc basalts and adakitic plutons. Gondwana Res. 15, 71–85.

McDonough, W.F., Sun, S.-S., 1995. Composition of the earth. Chem. Geol. 120, 223–253.

McReath, I., Faraco, M.T.L., 2006. Paleoproterozoic greenstone-granite belts in Northern Brazil and the former Guyana Shield e west African Craton province. Geol. Usp. Série Científica 5 (2), 49e63.

Mello, E.F., Xavier, R.P., McNaughton, N.J., Hagemann, S.G., Fletcher, I., Snee, L., 2006. Age constraints on felsic intrusions, metamorphism and gold mineralization in the Palaeoproterozoic rio Itapicuru greenstone belt, NE Bahia State, Brazil. Miner. Depos. 40, 849e866.

Meschede, M., 1986. A method of discriminating between different types of mid-ocean ridge basalts and continental tholeiites with the Nb-Zr-Y diagram. Chem. Geol. 16, 207–218.

Miyashiro, A., 1975. Classification, characteristics, and origin of ophiolites. J. Geol. 83, 249–281.

Oliveira, E.P., Mello, E.F., MacNaughton, N.J., 2002. Reconnaissance U–Pb geochronology of early precambrian quartzites from the Caldeirão belt and their basement, NE São Francisco craton, Bahia, Brazil: implications for the early evolution of the palaeoproterozoic Salvador–Curaçá orogen. J. South Am. Earth Sci. 15, 284–298.

Oliveira, E.P., Souza, Z.S., McNaughton, N., Lafon, J.M., Costa, F.G., Figueiredo, A.M., 2011. The Rio Capim volcanic-plutonic-sedimentary belt, Sãoo Francisco Craton, Brazil: geological, geochemical and isotopic evidence for oceanic arc accretion during Paleoproterozoic continental collision. Gondwana Res. 19 (3), 735e750.

Parente, C.V., Almeida, A.R., Arthaud, M.H., 2008. Geologia da folha Boa Viagem SB.24-V-D-II. Brasília: CPRM, 2008. Escala 1:100.000. Programa Geologia do Brasil - PGB.

Pearce, J.A., 2014. Immobile element fingerprinting of ophiolites. Elements 10 (2), 101–108.

Pearce, J.A., 1998. Mantle melting beneath island arcs: trace element constraints from basalts and peridotites. EOS 79, F992.

Pimentel, Marcio M., Silva, Maria da Gloria, 2003. Sm-Nd age of the Fazenda Brasileiro Gabbro, Bahia, Brazil: example of robust behavior of the Sm-Nd isotopic system under extreme hydrothermal alteration. An. Acad. Bras. Cienc. 75 (3), 383–392.

Pinéo, T.R.G., Costa, F.G., 2013. Dados aerogamaespectrométricos aplicados na delimitação do Complexo Cruzeta (Maciço Arqueano de Troia), Domínio Ceará Central da Província Borborema. In: 13° International Congress of the Brazilian Geophsical Society & EXPOGEf, Rio de Janeiro, Agosto de 2013.

Pires, A.C.B., Moraes, R.A.V., 2006. In: New processing technologies applied do airborne geophysical data: impact on interpretation. 2° Simpósio Brasileiro de Exploração Mineral, SIMEXMIN, (Ouro Preto, MG).

Polat, A., Hofmann, A.W., 2003. Alteration and geochemical patterns in the 3.7–3.8 Ga Isua greenstone belt, West Greenland. Precambrian Res. 126, 197–218.

Puchtel, I.S., Hofmann, A.W., Mezger, K., Jochum, K.P., Shchipansky, A.A., Samsonov, A.V., 1998. Oceanic plateau model for continental crustal growth in the Archaean: a case study from the Kostomuksha greenstone belt, NW Baltic Shield. Earth Planet. Sci. Lett. 155, 57–74.

Rosa Júnior, C.A., 2012. Aspectos Geológicos, Petrográficos e Geoquímicos das Rochas Metamáficas e Metaultramáficas da Sequência Metavulcano-Sedimentar Serra das Pipocas/CE. Relatório de Graduação. Universidade Federal do Ceará.

Rosa-Costa, L.T., Lafon, J.M., Delor, C., 2006. Zircon geochronology and Sm-Nd isotopic study: further constraints for the Archean and Paleoproterozoic geodynamical evolution of the southeastern Guiana Shield, north of Amazonian Craton, Brazil. Gondwana Res. 10 (3e4), 277e300.

Said, N., Kerrich, R., Cassidy, K., Champion, D.C., 2012. Characheristics and geodynamic setting of the 2.7Ga Yilgarn heterogeneous plume and its interaction with continental lithosphere: evidence from komatiite-basalt and basalt geochemistry of the Eastern Goldfilds Super terrane. Aust. J. Earth Sci. 59, 1–27.

Shervais, J.W., 1982. Ti-V plots and the petrogenesis of modern and ophiolitic lavas. Earth Planet. Sci. Lett. 59, 101–118.

Silva, L.C., Armstrong, R., et al., 2002. Reavaliação da Evolução Geológica em Terrenos Pré-Cambrianos Brasileiros com base em novos dados U-Pb SHRIMP. Parte III:

província Borborema, Mantiqueira Meridional e Rio Negro-Jurena. Rev. Bras. Geociencias 32, 529–544.

Silva, M.G., Coelho, C.E.S., Teixeira, J.B.G., Alves da Silva, F.C., Silva, R.A., Souza, J.A.B., 2001. The Rio Itapicuru greenstone belt, Bahia, Brazil: geologic evolution and review of gold mineralization. Miner. Depos. 36, 345e357.

Tassinari, W.S., Pellegrini, D., Carvalho, M.S., Sabroza, P., 2004. Space distribution of the leptospirosis in the City of Rio de Janeiro, Brazil, in the years of 1996–1999. Rep. Publ. Health 20, 1721–1729 (in Portuguese).

Thompson, R.N., 1982. Magmatism of the British Tertiary province Scottish. J. Geol. 18, 49–107.

Torres, P.F.M., Cavalcante, J.C., Palheta, E.S.M., Vasconcelos, A.M., Oliveira, F.V., 2007. Folha Quixadá. Folha SB-24-V-B, Escala 1:250.000. Geologia e Metalogênese. In: Programa Levantamentos Geológicos Básicos Do Brasil. Fortaleza: Serviço Geológico Do Brasil. CPRM.

Van Schmus, W. Rs, Brito Neves, B.B., Hackspacher, P.C., Babinski, M., 1995. U/Pb and Sm/Nd geocronological studies of the eastern Borborema Province, northeastern Brazil: initial conclusions. J. South Am. Earth Sci. 8 (3/4), 267–288.

Vanderhaeghe, O., Ledru, P., Thiéblemont, D., Egal, E., Cocherie, A., Tegyey, M., Milési, J.P., 1998. Contrasting mechanism of crustal growth: geodynamic evolution of the Paleoproterozoic granite-greenstone belts of French Guiana. Precambrian Res. 92 (2), 165e193.

Veríssimo, César Ulisses Vieira, Santos, Roberto Ventura, Parente, Clóvis Vaz, Oliveira, Claudinei Gouveia de, Cavalcanti, José Adilson Dias, Neto, Nogueira, de Araújo, José, 2016. The Itataia phosphate-uranium deposit (Ceará, Brazil) new petrographic, geochemistry and isotope studies. J. South Am. Earth Sci. 70, 115–144.

Wager, L.R., Deer, W.A., 1939. Geological investigations in East Greenland, pt. Ill: the petrology of the Skaergaard intrusion, Kangerdlugssuaq. East Greenland. Medd. om Grønland 105 (4), 1–335 Miyashiro, A. - 1975 - Metamorphism and metamorphic belts - 2~ ed. - UnWin Brothers Limited – Great Britain, 492 pp.

Whitney, D.I., Evans, B.W., 2010. Abbreviations for names of rock-forming minerals. Am. Mineral. 95, 185–187.

Winchester, J.A., Floyd, P.A., 1977. Geochemical discrimination of different magma series and their differentiation products using immobile elements. Chem. Geol. 20, 325–343.

Wood, D.A., Joron, J.L., Treuil, M., Norry, M., Tarney, J., 1979. Geochemistry of basic lavas from Iceland and surrounding ocean floor. Contrib. Mineral. Petrol. 70 (3), 319–339.